

A PSF-based Approach to TESS High quality data Of Stellar clusters (PATHOS) - III. Exploring the properties of young associations through their variables, dippers, and candidate exoplanets

D. Nardiello

▶ **To cite this version:**

D. Nardiello. A PSF-based Approach to TESS High quality data Of Stellar clusters (PATHOS) - III. Exploring the properties of young associations through their variables, dippers, and candidate exoplanets. Monthly Notices of the Royal Astronomical Society, 2020, 498, pp.5972-5989. 10.1093/mnras/staa2745 . insu-03667040

HAL Id: insu-03667040
https://insu.hal.science/insu-03667040

Submitted on 13 May 2022

HAL is a multi-disciplinary open access archive for the deposit and dissemination of scientific research documents, whether they are published or not. The documents may come from teaching and research institutions in France or abroad, or from public or private research centers.

L'archive ouverte pluridisciplinaire **HAL**, est destinée au dépôt et à la diffusion de documents scientifiques de niveau recherche, publiés ou non, émanant des établissements d'enseignement et de recherche français ou étrangers, des laboratoires publics ou privés.

Monthly Notices of the ROYAL ASTRONOMICAL SOCIETY

MNRAS **498,** 5972–5989 (2020) doi:10.1093/mnras/staa2745
Advance Access publication 2020 September 10

A PSF-based Approach to *TESS* High quality data Of Stellar clusters (PATHOS) – III. Exploring the properties of young associations through their variables, *dippers*, and candidate exoplanets

D. Nardiello [1,2]★

[1]*Aix Marseille Univ, CNRS, CNES, LAM, F-13013, Marseille F-13013, France*
[2]*Istituto Nazionale di Astrofisica - Osservatorio Astronomico di Padova, Vicolo dell'Osservatorio 5, IT-35122 Padova, Italy*

Accepted 2020 September 2. Received 2020 September 2; in original form 2020 July 31

ABSTRACT

Young associations in star-forming regions are stellar systems that allow us to understand the mechanisms that characterize the stars in their early life and what happens around them. In particular, the analysis of the discs and of the exoplanets around young stars allows us to know the key processes that prevail in their evolution and understand the properties of the exoplanets orbiting older stars. The *Transiting Exoplanet Survey Satellite* mission is giving us the opportunity to extract and analyse the light curves of association members with high accuracy, but the crowding that affects these regions makes difficult the light curve extraction. In the PATHOS project, cutting-edge tools are used to extract high-precision light curves and identify variable stars and transiting exoplanets in open clusters and associations. In this work, I analysed the light curves of stars in five young ($\lesssim$10 Myr) associations, searching for variables and candidate exoplanets. Using the rotational periods of the association members, I constrained the ages of the five stellar systems (∼2–10 Myr). I searched for *dippers*, and I investigated the properties of the dust that forms the circumstellar discs. Finally, I searched for transiting signals, finding six strong candidate exoplanets. No candidates with radius $R_{\rm P} \lesssim 0.9\ R_J$ have been detected, in agreement with the expectations. The frequency of giant planets resulted to be ∼2–3 per cent, higher than that expected for field stars ($\lesssim$ 1 per cent); the low statistic makes this conclusion not strong, and new investigations on young objects are mandatory to confirm this result.

Key words: techniques: image processing – techniques: photometric – planets and satellites: general – stars: variables: general – open clusters and associations: general.

1 INTRODUCTION

To date, more than 4000 exoplanets have been discovered and characterized,[1] but their properties have not always been those we observe today. Indeed, the exoplanets we observe were born with different properties: in their early life, planets are subject to a series of interactions with other bodies or the host star that cause changes in their orbital and physical parameters (migration, planetary impacts, atmospheric photoevaporation, etc.). All these processes have been studied in details (see e.g. Terquem & Papaloizou 2007; Ida & Lin 2010; Hansen & Murray 2012; Lopez & Fortney 2013; Owen & Wu 2013; Schlichting, Sari & Yalinewich 2015; Schlichting 2018) and partially explain some observables, like, e.g. the gap in the radius distribution of small planets at 1.5–2.0 $R_\oplus$ (Fulton et al. 2017; Fulton & Petigura 2018), the dearth of short-period giant planets in close-in exoplanet distribution (see e.g. Owen & Lai 2018 and references therein), and the accretion of the gaseous envelopes for giant planets (Baraffe et al. 2003; Marley et al. 2007; Spiegel & Burrows 2012; Mordasini, Marleau & Mollière 2017).

In order to understand all the mechanisms that prevail in the life of an exoplanet, it is mandatory to search for and monitor stars having different ages. Unfortunately, stellar age is one of the most difficult parameter to measure, unless the star is member of an association or of a star cluster (open or globular): in the latter cases, the age of the star can be well constrained because of the use of theoretical models. For this reason, the interest on these objects has grown in recent years and many photometric and spectroscopic works have been carried out on their members until now (e.g. Quinn et al. 2012; Meibom et al. 2013; Quinn et al. 2014; Malavolta et al. 2016; Pope, Parviainen & Aigrain 2016; David et al. 2016a; Mann et al. 2016b; Ciardi et al. 2018; Mann et al. 2018; Vanderburg et al. 2018; Benatti et al. 2019; Newton et al. 2019; Gaidos et al. 2020).

The *Kepler* (Borucki et al. 2010) and *K2* (Howell et al. 2014) missions were a success, allowing the detection of many exoplanets, also around stellar cluster and association members (Meibom et al. 2013; Barros, Demangeon & Deleuil 2016; Obermeier et al. 2016; Mann et al. 2016a; Libralato et al. 2016b; Nardiello et al. 2016b; Pepper et al. 2017; Curtis et al. 2018; David et al. 2019a,b), but their sky coverage was limited. The *Transiting Exoplanet Survey Satellite* (*TESS*; Ricker et al. 2015) mission is giving us the opportunity to study stellar cluster and association members with high photometric accuracy and unprecedented sky and temporal coverage: the satellite has probed more than 80 per cent of the sky in its first 2 yr of mission, observing a large fraction of stellar clusters and associations of the Galaxy for ∼27 d or more, and on 2020 July has started its extended mission. Given the low resolution of the *TESS* images and the high levels of

★ E-mail: domenico.nardiello@lam.fr
[1]https://exoplanetarchive.ipac.caltech.edu/

© 2020 The Author(s)
Published by Oxford University Press on behalf of the Royal Astronomical Society

Downloaded from https://academic.oup.com/mnras/article/498/4/5972/5903707 by guest on 13 May 2022

star crowding typical of clusters/associations, the extraction of high-precision light curves from *TESS* data needs appropriate techniques, such as the use of the difference imaging analysis (Bouma et al. 2019) or point spread function (PSF) models (Nardiello et al. 2019).

The project 'A PSF-based Approach to *TESS* High Quality data Of Stellar clusters' (PATHOS; Nardiello et al. 2019, hereafter Paper I) is aimed at finding and characterization of candidate exoplanets and variable stars in stellar clusters and associations, using high-precision light curves obtained with a cutting-edge tool based on the use of empirical PSFs and neighbour subtraction. This technique allows us to minimize the dilution effects due to neighbour contaminants, and extract high-precision photometry even for faint stars ($T \sim 17$–18). The efficiency of the method was demonstrated in Paper I: high-precision light curves of stars located in an extreme crowded region centred on the globular cluster 47 Tuc, containing also Galactic and Small Magellanic Cloud sources, were analysed. Many variables and one candidate hot Jupiter were identified. Using the same technique, Nardiello et al. (2020, hereafter Paper II) searched for exoplanets among the light curves of $\sim$ 163 000 stellar members of 645 open clusters observed during the first year of *TESS* mission, finding 11 strong candidates in eight open clusters with ages between $\sim$30 Myr and $\sim$2 Gyr.

In this third work of the series, I analysed the properties of the members of five young ($\lesssim$10 Myr) associations in as many star-forming regions using the light curves extracted from the images collected during the first year of the *TESS* mission. The analysed associations are Chamaeleon I, Chamaeleon II, Lupus, γ Velorum, and Corona Australis associations. Given their young ages ($\lesssim$10 Myr), these associations host a large number of T-Tauri pre-main-sequence stars, and for this reason they are also known as *T-associations*, term coined by Ambartsumian (1949) in his study on the importance of stellar associations for the understanding of the stellar formation and evolution. Today, the study of the properties of the young association members allows us not only to investigate the life of the stars, but also how circumstellar discs and exoplanets are born and evolved around them. Therefore, the analysis of the *TESS* light curves of young stellar objects (YSOs) in star-forming regions offers the unique opportunity to trace the origin and early evolution of circumstellar discs and exoplanets orbiting them. In the last years, a large number of studies concentrate their attention on young associations aimed to explore the metal content of their stars (e.g. James et al. 2006; González Hernández et al. 2008; Santos et al. 2008; D'Orazi et al. 2009; Biazzo et al. 2011, 2012a,b; D'Orazi, Biazzo & Randich 2011; Spina et al. 2014a,b; Jeffries et al. 2017), the discs that surround their young members (e.g. Chen et al. 2005; Carpenter et al. 2006, 2009; Chen et al. 2011; Luhman & Mamajek 2012; Ansdell et al. 2016; Bodman et al. 2017; Kuruwita et al. 2018; Bohn et al. 2019; Aizawa et al. 2020; Bredall et al. 2020), and the variability of the main-sequence stars (e.g. Rebull et al. 2018; Curtis et al. 2019; Rebull et al. 2020) in order to constraint their ages. Even if, in the last years, associations and stellar clusters have been the subjects of many exoplanet surveys, just a handful (candidate) exoplanets are known to orbit members of young ($\lesssim$100–150 Myr) clusters and associations, and just one exoplanet orbits a (pre-)main-sequence star in a $\lesssim$10 Myr old association, K2-33b (Upper Scorpius association, David et al. 2016b; Mann et al. 2016a). Other known exoplanets and candidates in young systems are the hot Jupiter HIP 67522 (Sco-Cen association, $\sim$17 Myr, Rizzuto et al. 2020), the planetary system around the star V1298 Tau (Tau-Aur association, $\sim$23 Myr, David et al. 2019b), the two candidate exoplanets PATHOS-30 and PATHOS-31 (IC 2602, $\sim$35 Myr, Paper II), the Neptune-size exoplanet DS Tuc Ab (Tuc-Hor association $\sim$40 Myr, Newton et al. 2019; Benatti et al. 2019), and the sub-Neptune EPIC 247267267b (Cas-Tau group, $\sim$120 Myr, David et al. 2018).

In this work, the PATHOS pipeline is used to extract and correct the *TESS* light curves of a sample of likely young association members (Section 2). Variable stars have been identified in order to constraint the association ages and analyse the dust in the circumstellar discs around YSOs (Section 3). The discovery and characterization of new candidate exoplanets orbiting stars in the aforementioned associations and their frequency is reported in Section 4. Section 5 is a summary and a discussion of the results obtained in this work.

2 OBSERVATIONS AND DATA REDUCTION

In this work, I extracted the light curves of the stars in five very young associations observed during the first year of the *TESS* mission. In particular, I used full frame images (FFIs) collected during Sectors 7, 8, 9, 11, 12, and 13. I produced a total of 7150 light curves associated with 4459 stars. The pipeline adopted for the light-curve extraction and correction is widely described in Papers I and II. The pipeline includes the use of the light-curve extractor `IMG2LC`, developed by Nardiello et al. (2015a, 2016a) for ground-based images and improved by Libralato et al. (2016a,b) and Nardiello et al. (2016b) for *Kepler/K2* space-based data. Briefly, the routine uses empirical PSFs and an input catalogue (see Section 2.1) to extract aperture and PSF-fitting photometries of each star in the catalogue after the subtraction of all the neighbours from each *TESS* FFI. The raw light curves are then corrected for systematic effects by fitting and applying to them the Cotrending Basis Vectors described in Paper II. Light curves will be released in `ascii` and `fits` format on the Mikulski Archive for Space Telescopes (MAST) as a High Level Science Product (HLSP) under the project PATHOS[2] (DOI: 10.17909/t9-es7m-vw14). A description of the format of the light curves is reported in Papers I and II and in the MAST webpage of the PATHOS project.

2.1 The input catalogue

In this work, I analysed stars that have high probability to be members of five associations: Chamaeleon I and II associations (hereafter, ChI and ChII), Lupus association (Lup), Corona Australis association (CrA), and γ Velorum association (Vel). The selection of likely association members was performed using *Gaia* DR2 (Gaia Collaboration 2018) information, such as proper motions and parallaxes. For each association, I extracted from the *Gaia* DR2 catalogue all the stars with $G < 19$, within circular regions (of radius r_0) of the sky centred in the (α_0, δ_0); the values of r_0, α_0, and δ_0 are tabulated in Table 1. For each region, I first analysed the proper motion distributions of the stars with $G < 15$, and I selected manually the area of the vector-point diagram where likely association members are located. I fitted the $\mu_\alpha \cos\delta$ and μ_δ distributions with Gaussian functions, and I selected all the points within 3.5σ from the mean values of $\mu_\alpha \cos\delta$ and μ_δ. I fitted the parallax (π) distribution of the selected stars with a Gaussian, and I selected all the points within 3.5σ from the mean value of π. I iterated the procedure 10 times, alternating the proper motion and parallax selections and using only the stars that passed the selection criteria of the previous iteration. An example of likely association member selection for the CrA is illustrated in Fig. 1. The Vel and Lup associations are more complex systems and are formed by groups of stars having slightly different kinematical properties; in particular, in the vector-point diagram association stars form different close clumps. When possible, I fitted all the

[2] https://archive.stsci.edu/hlsp/pathos

Downloaded from https://academic.oup.com/mnras/article/498/4/5972/5903707 by guest on 13 May 2022

Table 1. Association information.

Association Name	α_0 (deg)	δ_0 (deg)	r_0 (deg)	$\mu_\alpha \cos\delta$ (mas yr^{-1})	μ_δ (mas yr^{-1})	π (mas)	[Fe/H][a]	N
ChI	166.70	−77.30	7.0	−22.4 ± 1.4	+0.5 ± 2.1	5.22 ± 0.15	−0.08 ± 0.04	191
ChII	193.41	−77.17	7.0	−20.2 ± 2.8	−7.5 ± 2.7	5.04 ± 0.13	−0.11 ± 0.14	50
Lup	240.00	−38.25	25.0	−11.5 ± 0.6	−21.8 ± 0.6	5.42 ± 1.24	−0.10 ± 0.04	3105
Vel	122.34	−47.35	10.0	−5.4 ± 0.9	+8.7 ± 0.9	2.53 ± 0.31	−0.06 ± 0.02	2895
CrA	285.46	−36.98	15.0	+1.2 ± 3.3	−27.2 ± 1.6	6.61 ± 0.28	−0.04 ± 0.05	388

[a] Metallicities from James et al. (2006), Spina et al. (2014a,b).

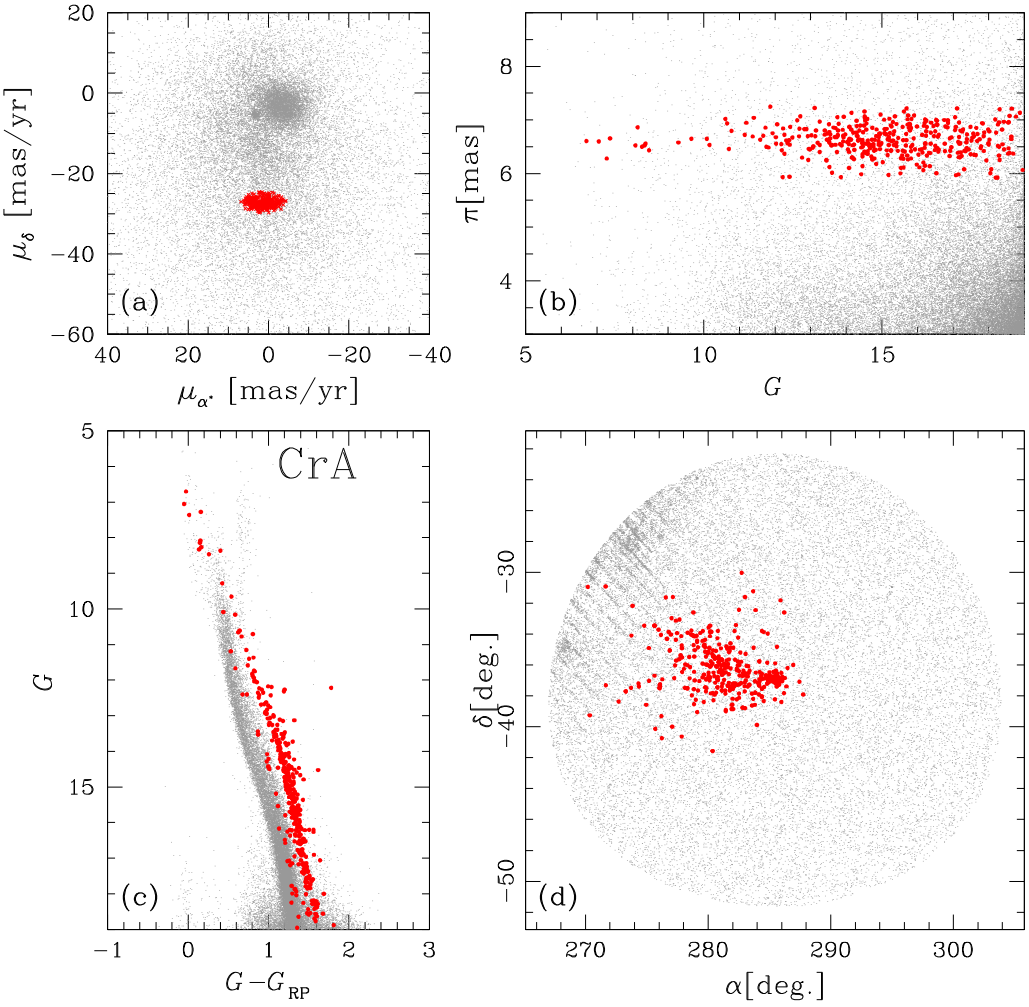


Figure 1. Overview on the selection procedure of likely CrA association members. Panel (a) shows the vector-points diagram of proper motions for the stars in the circular region ($r_0 = 15.0$ deg) of the sky centred on (α_0, δ_0) = (285.46, −36.98); panel (b) is the parallax distribution of the same stars as a function of the G magnitude; panels (c) and (d) show the G versus ($G - G_{RP}$) CMD and the (α, δ) positions for the stars in the considered region. The red and the grey points represent the likely association members and the discarded stars in the selection procedure, respectively. In all the panels, for clarity, only 20 per cent of the discarded stars are plotted.

single clumps with Gaussian functions and I selected the stars as previously described. The final catalogue given as input of `IMG2LC` contains 6629 stars. I cross-matched the final catalogue with the TIC v8 catalogue (Stassun et al. 2019), in order to obtain photometric information on all the stars. In particular, I included in the catalogue (in addition to *TESS* and *Gaia* magnitudes) the magnitudes in *B*- and *V*-Johnson bands, the 2MASS *J*, *H*, and K_s magnitudes (Cutri et al. 2003), and the infrared WISE (Wright et al. 2010) magnitudes *W*1 ([3.4 μm]), *W*2 ([4.6 μm]), *W*3 ([12 μm]), and *W*4 ([22 μm]). Reddening values [$E(B - V)$] were extracted for each star in the input catalogue using the PYTHON routine `mwdust`[3] implemented by Bovy et al. (2016), and the `Combined19` dustmap (Drimmel, Cabrera-Lavers & López-Corredoira 2003; Marshall et al. 2006; Green et al. 2019). Fig. 2 shows an example G versus ($G - G_{RP}$) colour–magnitude diagram (CMD) before panel (a) and after panel (b) the correction for reddening for the two close associations ChI and ChII.

[3] https://github.com/jobovy/mwdust

Downloaded from https://academic.oup.com/mnras/article/498/4/5972/5903707 by guest on 13 May 2022

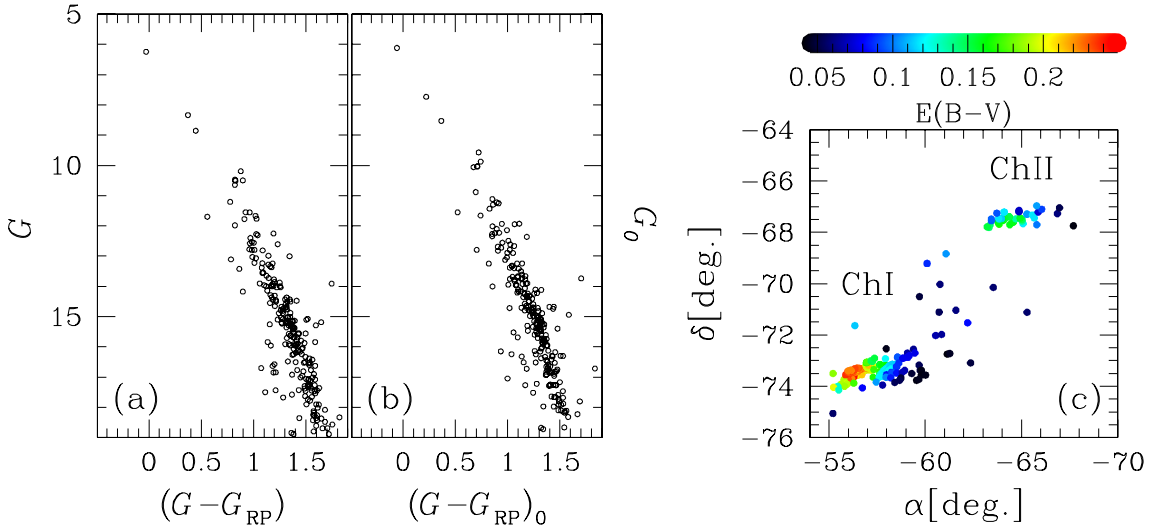


Figure 2. Reddening correction for the associations ChI and ChII based on the dust-map released by Bovy et al. (2016). Panels (a) and (b) show the G versus $(G - G_{RP})$ CMD before panel (a) and after panel (b) the correction. Panel (c) shows the reddening map for the two associations.

2.2 Photometric precision

Following the same methodology as in Papers I and II, I calculated the following quality parameters for the cotrended light curves: (i) the photometric `RMS`, defined as the 68.27th percentile of the sorted residual from the 3.5σ-clipped median value of the light curve because the simple photometric `RMS` is very sensitive to stellar variations, I calculated the (ii) `P2P RMS`, defined as the 68.27th percentile of the sorted residual from the median value of the vector $\delta F_i = F_i - F_{i+1}$, where F is the flux value at a given epoch i. I fitted the `RMS` and `P2P RMS` distributions with different polynomial functions, changing the order between $n = 1$ and $n = 5$, to derive the best mean trend of each photometric method. I found that, on average, the best fit was the one with $n = 2$. Fig. 3 shows the `RMS` (top panel) and `P2P RMS` (bottom panel) distributions; the coloured lines are the second-order polynomial fits performed for each photometric method. As done in Paper II, I used the `P2P RMS` trends to define the best photometric method for each light curve: for not saturated stars with $T \lesssim 7.0$, I used stars extracted with the 4-pixel aperture photometry; in the $7.0 \lesssim T \lesssim 9.5$ regime, 3-pixel aperture photometry gives the best results; for stars having $9.5 \lesssim T \lesssim 11.0$ the 2-pixel aperture photometry produces, on average, light curves with the lower `P2P RMS`; PSF-fitting photometry works better than the aperture photometry in the range $11.0 \lesssim T \lesssim 14.5$; in the faint regime, $T \gtrsim 14.5$, the best choice is the 1-pixel aperture photometry.

After this first selection, to exclude stars contaminated by different kind of sources (bleeding columns, bad pixels, not-subtracted stars, blended stars), I excluded all the sources for which the mean instrumental magnitude T_{instr} is too different from that expected knowing the calibrated T_{cal}. In order to select the best stars, I calculated the mean of the $\delta T = T_{instr} - T_{cal}$ distribution, $\delta\bar{T}$, and its standard deviation $\sigma_{\delta T}$ and I excluded all the stars for which $|\delta T - \delta\bar{T}| > 4 \times \sigma_{\delta T}$; 4088 stars passed all the selection criteria and have been analysed.

3 STELLAR VARIABILITY

The analysis of the stellar variability of the association members is crucial to constraint some properties of the associations.

In order to find periodic variable stars, I used the generalized Lomb–Scargle (GLS; Zechmeister & Kürster 2009) routine implemented in `VARTOOLS 1.38`[4] (Hartman & Bakos 2016) to extract the periodograms of the light curves. After the identification of the period associated with the most powerful peak in the periodogram, the routine whitened the light curve and extracted the periodogram of the light curve again to find the second strongest peak period. The reasons for this multiperiod finding are (i) some stars present multiple signals associated with different physical phenomena (see e.g. Rebull et al. 2016), and the multiperiod finding allows us to identify the different periods; (ii) artefacts in the light curve or effects due to the observations (sampling, temporal gaps in the light curve, outliers, etc.) might generate a peak in the periodogram stronger than that associated with the real physical signal coming from the star; multiple-period finding allows us to recover the real signal. For each light curve, I searched for periods between 0.08 d $\leq P \leq T_{LC}$, where T_{LC} is the maximum temporal baseline of the light curve. I excluded the candidate variable stars blended with other stars in the catalogue having similar signals using the routine `findblends` implemented in `VARTOOLS 1.38`: this routine compares the positions of the stars in a catalogue, their periods found using GLS periodograms and the amplitudes of their light curves to find blended stars. I used the signal-to-noise ratio (SNR) parameter to isolate the candidate variable stars following the method described in Nardiello et al. (2015a) and shown in Fig. 4: I divided the SNR distribution in intervals of $\delta P = 1$ d, and I computed the 3.5σ-clipped mean and standard deviation of the SNR values inside each bin. I interpolated the points 3σ above the mean SNR values with a spline, and I considered as candidate variables the points above the interpolated line (orange points in panels (a) and (b) of Fig. 4). I applied this procedure both to the SNR distributions associated with the first peak of the periodograms and to the SNR associated with the second peak periods; I considered as candidate variables the stars selected in both the sample (2230 stars). Finally, I visually inspected the phased light curves to assign to each candidate variable star the corrected period (or both the periods if the star have multiple periods), or to discard it because false positive. Panels (c), (d), and (e) show an example of light

[4]https://www.astro.princeton.edu/~jhartman/vartools.html

Downloaded from https://academic.oup.com/mnras/article/498/4/5972/5903707 by guest on 13 May 2022

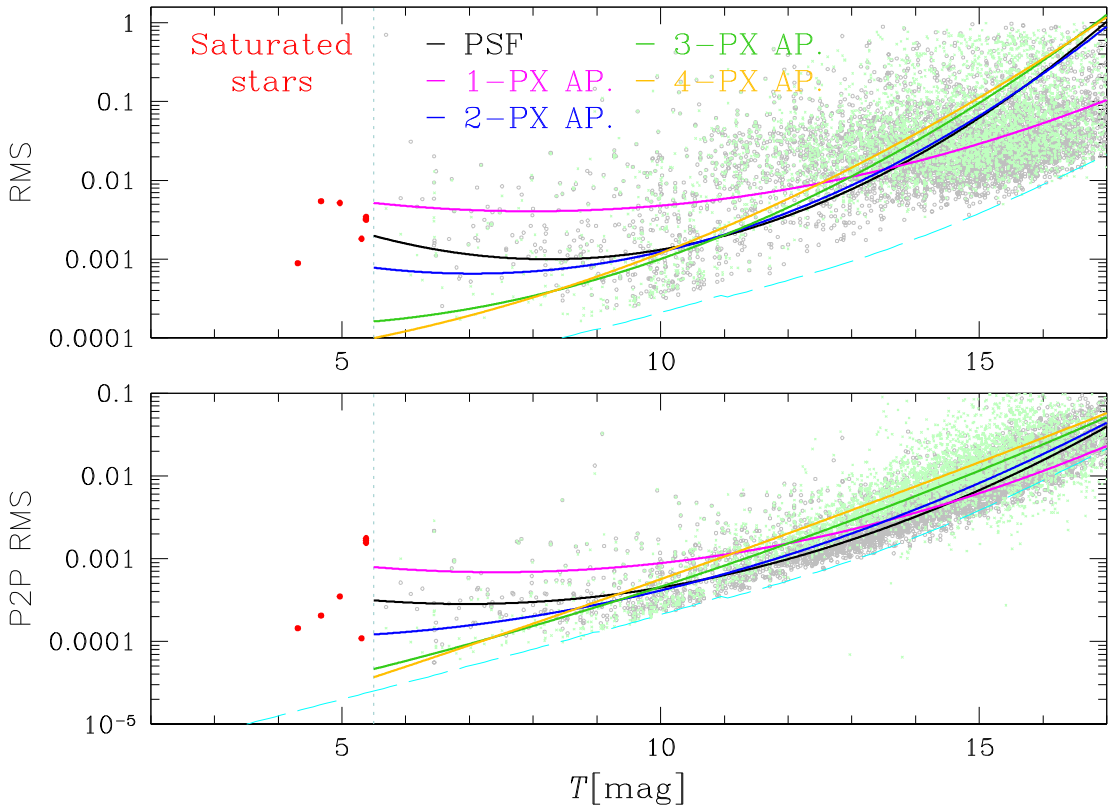


Figure 3. Photometric RMS and P2P RMS distributions as a function of the *TESS* magnitude for the light curves extracted in this work. The coloured lines represent the second-order polynomial interpolation to the RMS distributions: black for PSF-fitting photometry, magenta, blue, green, and yellow for 1-px, 2-px, 3-px, and 4-px aperture photometries, respectively. The light blue dashed line represents the theoretical limit. The grey dots and the light green crosses are examples of RMS distributions for PSF-fitting and 3-px aperture photometries, respectively. The red points are the saturated stars.

curve of a star characterized by multiple periods. The final list of periodic variable stars contains 1260 stars, 28 of them have multiple periods. A list of periodic variable stars used in this work is available electronically. The description of the columns are reported in Table A1.

3.1 Period–colour distribution analysis

Because of their young age and of the low number of members, the estimation of the association ages based on the use of theoretical models is not immediate. Using gyrochronology, i.e. the method for the estimation of the age based on the analysis of stellar rotation and magnetic braking (Barnes 2003, 2007), it is possible to constraint the age of the associations studied in this work.

In this work, I combined the period–colour distribution analysis and the CMD isochrone fitting, in order to constraint the age of each association and use this parameter in the characterization of the candidate transiting exoplanets (Section 4). In a first step, I found a raw estimation of the ages of the five associations comparing the period-$(V-K_s)_0$ dereddened colour distributions of the associations studied in this work with that obtained by Rebull et al. (2018) for the ρ Oph (∼1 Myr) and Upper Sco (∼8 Myr) associations, and with the period–colour analysis performed by Rebull et al. (2020) for the Taurus association (∼3 Myr). I used this first guess on the age to perform a fit of the isochrones and extract the age of each association. The associations studied in this work have a slightly subsolar metallicity ([Fe/H] ∼ −0.10 – −0.05, see e.g. James et al. 2006; Spina et al. 2014a,b; Table 1). For the isochrones fitting I used two sets of metallicities: for ChI, ChII, and Lup associations I used isochrones with [Fe/H] = −0.10, while for Vel and CrA isochrones with [Fe/H] = −0.05.

(i) ChI & ChII associations. Because of the low number of members and because the two associations are almost coeval and at the same distance (∼195 pc), I analysed their period–colour distributions together. Panel (a_1) of Fig. 5 shows the P versus $(V-K_s)_0$ distributions for ChI & ChII (the black points) compared to that of ρ Oph (the red points) and Taurus (the green points) associations: in the four associations low-mass slow-rotator (P ∼ 2–10 d) stars prevail. It means that all the associations are almost coeval. The associations ρ Oph and Taurus are very young with ages between ∼1 and ∼3 Myr (Rebull et al. 2018, 2020). I used this information to constraint the fit of the isochrones shown in panel (b_1). I computed the median reddening $E(B-V)$ and the median distance modulus[5] $(m-M)_0$ of the stars that belong to ChI and ChII associations, and I performed a χ^2-fit of a set of PAdova and TRieste Stellar Evolution Code (PARSEC; Girardi et al. 2002; Bressan et al. 2012; Marigo et al. 2017) isochrones [6] with ages that run from 1 to 5 Myr, in step of 0.5 Myr, to the G versus $(G-G_{RP})$ CMD, as done by Nardiello et al. (2015b, I refer the reader to this work for a detailed description of the fit procedure). I found that the best fit is associated with an age of 2.5 ± 1.0 Myr.

[5]Using the *Gaia* DR2 parallaxes corrected for the −30 μmas offset found by Lindegren et al. (2018).
[6]http://stev.oapd.inaf.it/cgi-bin/cmd

Downloaded from https://academic.oup.com/mnras/article/498/4/5972/5903707 by guest on 13 May 2022

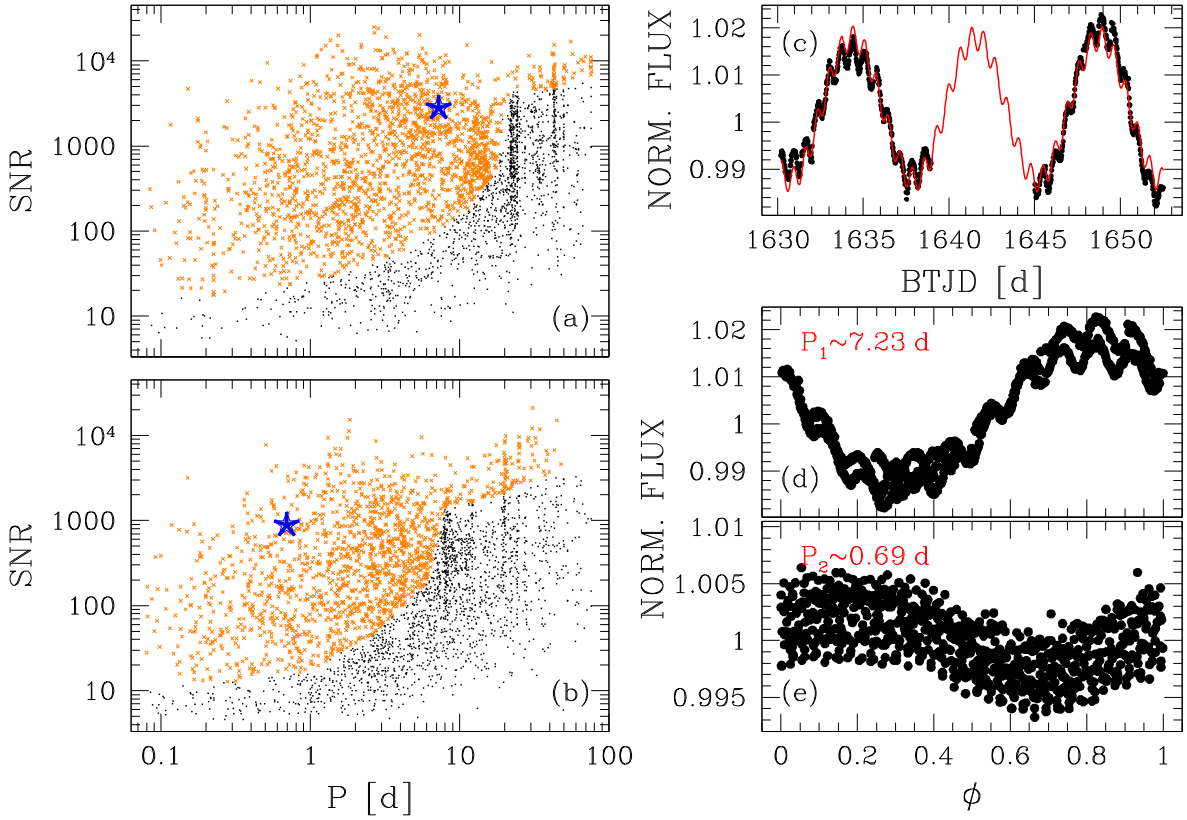


Figure 4. Selection of candidate variable stars. Panels (a) and (b) show the selection of candidate variables in the SNR versus Period plane, for the first and the second peak period, respectively: the orange points are the candidate variables selected on the basis of their SNR; the blue starred point represent the star TIC 69420071 whose light curve is shown in panel (c). In red is the sinusoidal model obtained combining the two peak periods found by GLS. Panel (d) shows the light curve of TIC 69420071 phased adopting the first peak period (∼7.23 d); panel (e) shows the (whitened) light curve phased using the second peak period (∼0.69 d).

(ii) Lup association. Even if I performed strict selections on proper motions and parallaxes for the groups that form the complex Lup association, some field stars are still present in the catalogue. In the analysis of variable stars, I excluded these likely field stars on the basis of their colours and magnitudes. Panel (a_2) of Fig. 5 shows the period–colour distribution of variable stars in the Lup association compared to that derived by Rebull et al. (2018) for Upper Sco stars (the empty black circles are the likely field stars). The two distributions are very similar, with a scattered sequence of AFGK stars that become slower as the mass decreases, and a well-populated sequence of M stars, whose periods decrease from early to late spectral types. The age of Upper Sco is ∼8–10 Myr (Pecaut, Mamajek & Bubar 2012; Rebull et al. 2018): starting from this constraint, I performed a fit of isochrones (with ages between 5 and 15 Myr) to the Lup association CMD [panel (b_2) of Fig. 5]. The best fit is obtained for an age of 8.0 ± 2.0 Myr.

(iii) Vel association. Because the Vel association is further away than the other associations studied in this work, low-mass stars have luminosities over the *TESS* magnitude limit and the result is that the period–colour distribution is cut on the red part, as shown in panel (a_3) of Fig. 6. Even if the sequence of M dwarfs is incomplete, the sequence formed by AFGK stars (which periods increases with the colour) and part of the sequence of M-type stars are very similar to that of the Upper Sco association. As done for the Lup association, I used a set of isochrones with ages between 5 and 15 Myr to search the age that gives the best fit. I found an age of 10.0 ± 3.0 Myr, as shown in panel (b_3) of Fig. 6

(iv) CrA association. The period–colour distribution of variable stars in the CrA association is shown in panel (a_4) of Fig. 6, compared to the distributions of Taurus and Upper Sco stars. The distribution of the periods of the M stars in the CrA association follows that of the M stars in the Upper Sco, with late-type stars that are faster rotators than early M dwarfs. Unfortunately, few stars with spectral types earlier than M populate the period–colour distribution, and a direct comparison of this part of the distribution is not possible. Using these information, I performed a fit of the CMD using isochrones with ages between 1 and 15 Myr; I found the best fit for an age of 6.0 ± 2.0 Myr [panel (b_4) of Fig. 6].

3.2 Dipper stars and disc properties

Young stellar systems, like the associations analysed in this work, host low-mass ($\lesssim 1 M_{\odot}$) T Tauri-like 'dipper' stars surrounded by circumstellar discs. Dipper stars are YSOs that show dimming events (periodic or not) in their light curves, probably caused by the dust located in the inner regions of a circumstellar disc that 'transits' on the stellar disc (Bodman et al. 2017). The luminosity of these stars usually decreases between few percent to >1 magnitude, on time-scales between few hours and about 1 d.

Characterize dipper stars and their discs in young associations with different ages is essential to understand how they evolve and which are the cleaning time-scales of discs, allowing us to constraint the models on the planet formation.

To date, few ground-based surveys have been performed to study these objects (see e.g. Cody & Hillenbrand 2010; Morales-Calderón

Downloaded from https://academic.oup.com/mnras/article/498/4/5972/5903707 by guest on 13 May 2022

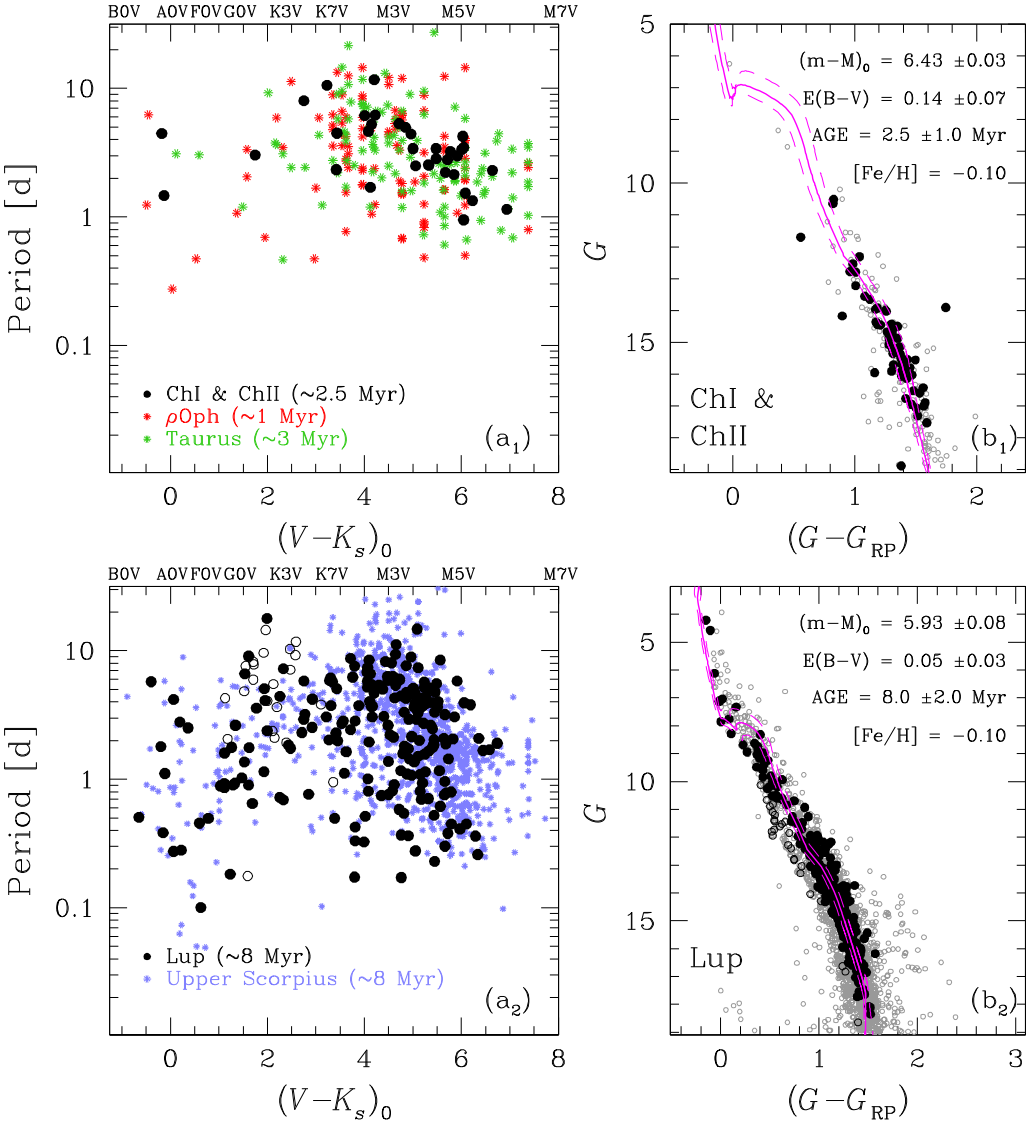


Figure 5. Age computation of the associations studied in this work based on the analysis of Period-$(V-K)_0$ distributions and on the fit of the isochrones. Panels (a) show the Period-$(V-K)_0$ for one of the associations studied in this work (in black) compared to the distributions obtained for other associations in other works (ρ Oph, Taurus, and Upper Sco in red, green, and violet, respectively, Rebull et al. 2018, 2020). On the top of the panels (a) are reported the spectral classes as defined by Pecaut & Mamajek (2013, table updated to 2019 March). Panels (b) show the best-fitting isochrones to the G versus $(G-G_{RP})$ CMD of the single associations and the parameters used to obtain the fit. In this figure, the results for ChI, ChII (top panels), and Lup associations (bottom panels, the empty black circles indicate likely field stars) are shown.

et al. 2011); in the last years data from telescopes in space (*K2/Kepler* and *CoRot*), gave a great contribution to the analysis of dipper stars (see e.g. Stauffer et al. 2015; Ansdell et al. 2016; Rodriguez et al. 2017; Cody & Hillenbrand 2018), but these missions had very limited sky coverage. Recently, Bredall et al. (2020) characterized 11 stars in the Lupus region, combining ground-based (ASAS-SN) and space-based (*TESS*) data. In fact, *TESS* is offering a unique opportunity to study with an high photometric accuracy the evolution of the light coming from these stars, over a long time baseline ($\gtrsim$1 month).

In this Section, I describe the procedure I followed to search and characterize the dippers among the association members for which I extracted the *TESS* light curves.

In order to search for dipper stars, I used three different metrics: (i) the RMS, sensitive to the scatter of the light curve; (ii) the peak-to-peak variability metric (ν), as defined by Sokolovsky et al. (2017), that is sensitive to the variability of the star in general; (iii) the Flux Asymmetry (M), defined by Cody et al. (2014) and Cody & Hillenbrand (2018), sensitive to fading/brightening events in the light curve. First, I divided the RMS distribution in bin of 1.0 T-magnitude, and, within each interval, I computed the mean $\bar{RMS}$ and the standard deviation of the $\sigma_{\bar{RMS}}$; I interpolated the $\bar{RMS} + 3 \times \sigma_{\bar{RMS}}$ points with a cubic spline and I selected all the sources above the interpolation. I performed the same procedure using as parameter ν, and I discarded all the points that were not selected in RMS and ν selections and having $M < -0.25$. I visually checked the light curves of the 652 stars that passed the selection, identifying 71 candidate dippers (>90 per cent associated with stars of spectral-type K and M).

Following the procedure adopted by Bredall et al. (2020), I used the All-Sky Automated Survey for SuperNovae (ASAS-SN; Shappee et al. 2014; Kochanek et al. 2017) g-band light curves to calculate the ratio between the extinction coefficient A_T in T band and that in g-sloan band, A_g. This quantity is strictly linked to the grain size of the

Downloaded from https://academic.oup.com/mnras/article/498/4/5972/5903707 by guest on 13 May 2022

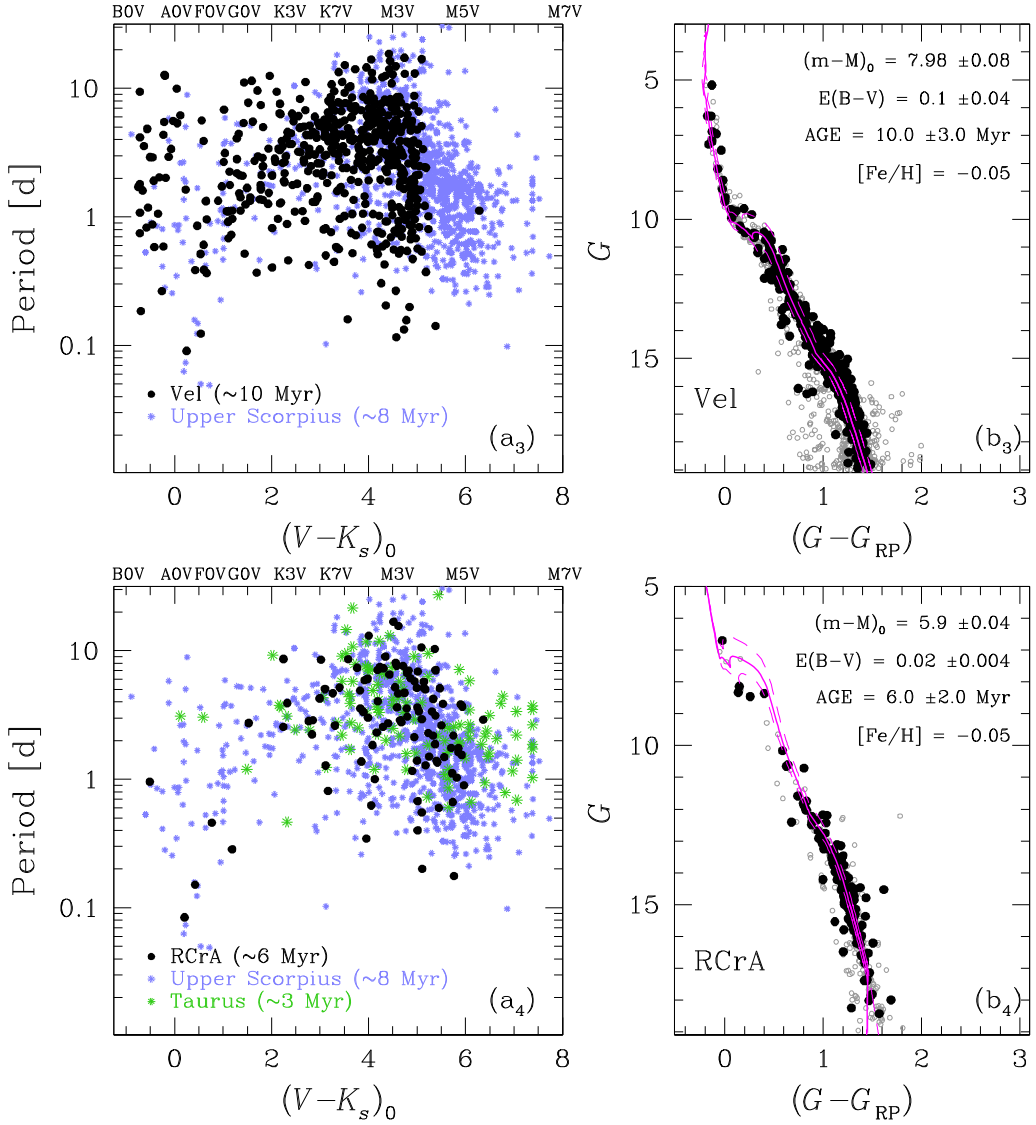


Figure 6. As in Fig. 5, but for Vel (top panels) and CrA (bottom panels) associations.

dust that surrounds the star. Defining δT and δg the dimming of the *TESS* and ASAS-SN light curve, the quantity $\Delta(\delta g - \delta T)$ represents the reddening $E(g - T) = A_g - A_T$ caused by the dust. Therefore,

$$\frac{\Delta(\delta g - \delta T)}{\delta g} = \frac{A_g - A_T}{A_g} = 1 - \frac{A_T}{A_g} \quad (1)$$

and the quantity A_T/A_g can be inferred measuring the slope of the $\Delta(\delta g - \delta T)$–$\delta g$ relation. I downloaded from the ASAS-SN archive[7] the g-band light curves for all the dippers having $T < 14.5$ (53 stars), with a baseline that covers the *TESS* observational period of the first year of mission. Panels (a) of Fig. 7 show two examples of light curves of dippers observed for two consecutive *TESS* sectors by *TESS* (the grey points) and ASAS-SN (the green points). I extracted the relationship between $\Delta(\delta g - \delta T)$ and δg splitting the light curves in sub-sectors, each one ending with the *TESS* down-link of the data (about every 13.5 d): in this way I avoid (second-order) systematic effects due to the variation of the photometric zero-point between the first and second part of a sector. Panels (b) shows $\Delta(\delta g - \delta T)$ as a function of δg for the two stars showed in panels (a): I performed a linear least-squares fit to the data of each sub-sector to obtain the slope $(1 - A_T/A_g)_i$, with $i = 1, ...N_{\rm ssec}$ is ith sub-sector, and, finally, I averaged all the slopes. The fits obtained with the mean slope are shown in panels (b) of Fig. 7 (the red lines). The catalogue of the identified dippers and of the A_T/A_g values is released as electronic material; Table A2 reports the description of this catalogue.

The ratio A_T/A_g gives information about the size of the grains that form the surrounding disc: if the dust is dominated by small grains, the quantity A_T/A_g will be smaller than the case in which the grains have large size; if the size of the grains are larger than the wavelengths in which the *TESS* observations were performed ($\lambda_{\rm central} \sim 800$ nm), the ratio $A_T/A_g \to 1$, and the reddening $E(g - T) = A_g - A_T \to 0$.

Panel (c_1) of Fig. 7 shows the A_T/A_g as a function of the dereddened colour $(V - K_s)_0$: the two quantities are slightly correlated (Pearson coefficient ~ -0.4), with, on average, earlier type stars having discs formed by larger grains. Bredall et al. (2020) found a weak relation between the grain sizes and the infrared excess measured with the colour (K_s − [22 μm]), with the infrared excess that inversely

[7] https://asas-sn.osu.edu/

Downloaded from https://academic.oup.com/mnras/article/498/4/5972/5903707 by guest on 13 May 2022

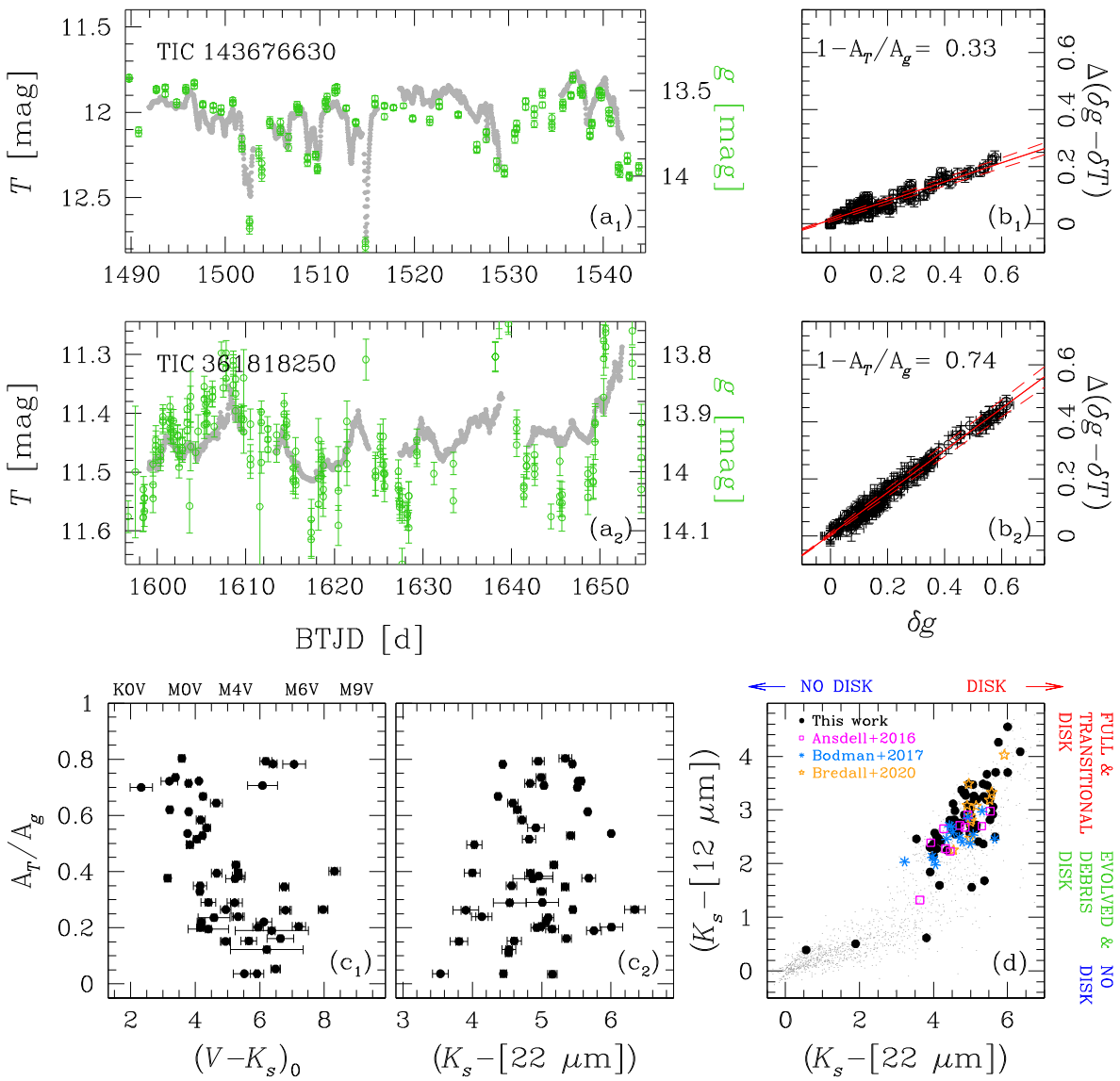


Figure 7. Analysis of the dippers. Panels (a) show two example of light curves of dipper stars obtained using *TESS* data (the grey points) and ASAS-SN g-band data (the green points); the magnitude limits on the y-axis cover the same interval for T and g magnitudes, in order to directly compare light curves obtained with different instruments. Panels (b) show the $\Delta(\delta g - \delta T)$ versus δg diagram: the red lines are the best least-squares fit. The slope of the fitted line is correlated to the reddening caused by the circumstellar disc and is related to the size of the grains that form the dust. Panel (c_1) is the A_T/A_g versus the dereddened colour index $(V - K_s)_0$ diagram: on the top are reported the spectral classes as defined by Pecaut & Mamajek (2013; table updated to 2019 March). Panel (c_2) shows A_T/A_g versus the infrared excess indicator $(K_s - [22\ \mu m])$. Panel (d) is the $(K_s - [12\ \mu m])$ versus $(K_s - [22\ \mu m])$ colour–colour diagram as reported by Luhman & Mamajek (2012): the different evolutionary stages of the disc are reported on the right. The grey points are all the stars in the input catalogue adopted in this work, the black-filled circles are the dipper stars identified in this work, the magenta empty squares, the azure asterisks, and the orange stars are the dippers identified by Ansdell et al. (2016), Bodman et al. (2017), and Bredall et al. (2020), respectively.

decreases with the dimension of the grains. Panel (c_2) of Fig. 7 illustrates the distribution of the A_T/A_g measured in this work as a function of the infrared excess $(K_s - [22\ \mu m])$: it shows that there is not a clear correlation between the two quantities (Pearson coefficient: ∼0.3), and it does not confirm what found by Bredall et al. (2020).

The presence of a disc around the dippers found in this work is also confirmed by the analysis of the excess emission in infrared shown in panel (d) of Fig. 7. In fact, the evolutionary stage of a disc can be inferred comparing the stellar luminosity in the 2MASS K_s band with its WISE infrared magnitudes. As reported by Luhman & Mamajek (2012), in a $(K_s - [12\ \mu m])$ versus $(K_s - [22\ \mu m])$ colour–colour diagram, stars with $(K_s - [22\ \mu m]) \gtrsim 3.2$ are surrounded by *full/transitional* discs,[8] while *evolved* and *debris* discs are located in the area defined by $(K_s - [22\ \mu m]) \gtrsim 3.2$ and $(K_s - [12\ \mu m]) \gtrsim 0.5$. Stars with small values of the colour–colour indexes (∼0) have no disc. Panel (d) of Fig. 7 confirms that the large part of YSOs-dippers found in this work have *full* or *transitional* discs; about five objects have *evolved* or *debris* discs. For completeness, I also report the results by Ansdell et al. (2016), Bodman et al. (2017), and Bredall et al. (2020). I found that about half of dippers found in this work are

[8]I refer the reader to Luhman & Mamajek (2012) for a detailed description of the different evolutionary stages of the discs.

Downloaded from https://academic.oup.com/mnras/article/498/4/5972/5903707 by guest on 13 May 2022

located in the ChI and ChII associations (23 and 14, respectively) and the other half in the Lup, CrA, and Vel associations (19, 5, and 10, respectively). Considering the number of stars for which I studied the light curves, I found that in the very young associations ChI and ChII (∼2.5 Myr) there is a high fraction of dippers (∼12 per cent and ∼28 per cent, respectively), while the the fraction of dippers decreases considering the other older associations: Lup and CrA (∼6-8 Myr) associations contain ∼1−2 per cent of dipper stars, while in the Vel association (∼10 Myr) only ∼0.4 per cent of analysed stars are dippers, confirming that discs around low-mass stars (∼0.1–0.5 $M_{\odot}$) survive up to 10 Myr (see e.g. Carpenter et al. 2009; Luhman & Mamajek 2012).

4 CANDIDATE EXOPLANETS

I searched for candidate exoplanets among the association members using the procedure described in Paper II. In order to search for transits in the light curves, stellar variability must be removed from them. I modelled the variability of each light curve interpolating to it a fifth-order spline defined on $N_{\rm knots}$. I considered three different grids of knots (with knots every 4.0, 6.5, and 13.0 h) to better model the light curve of short- and long-period variable stars and also to avoid the flattening of transits whose duration is longer than 4 or 6.5 h. I removed bad photometric measurements from the flattened light curves by clipping away all the outliers 4σ above the median flux, and discarding all the points with `DQUALITY > 0` and values of the local background 5σ above the mean background value.

Adopting the routine developed by Hippke & Heller (2019), I extracted the transit-fitting least-squares (TLS) periodograms[9] of the flattened and 'cleaned' light curves. I searched for transits with period 0.6 d $\leq P < 0.5 \times T_{\rm LC}$, where $T_{\rm LC}$ is the maximum temporal interval covered by the light curve. I performed a first selection of candidate transiting objects on the basis of four parameters extracted by the TLS routine: (i) the signal detection efficiency (SDE), (ii) SNR, (iii) the significance between odd and even transits ($\sigma_{\rm odd-even}$), and (iv) the mean depth of the transits ($\delta_{\rm t}$). I selected as candidates all the stars having (i) SDE ≥ 9 [panel (a_1) of Fig. 8], (ii) SNR ≥ 5 [panel (a_2) of Fig. 8), (iii) $\sigma_{\rm odd-even} < 3$, and (iv) $\delta_{\rm t} < 10$ per cent. I visually inspected the light curves that passed the selections to check the odd/even transit depths [panels (c) of Fig. 8], the presence of secondary eclipses, and to exclude false positives due to the presence of artefacts in the light curves. For each sector, I applied this procedure to the light curves flattened using the three different grids of knots previously described. I repeated this procedure considering as a first step each sector independent from the others, and then considering the stacked light curves of the stars observed in more than one sector: in this way I avoided that possible artefacts in (or different photometric precision of) the light curves of stars observed in more than one sector decrease the detection efficiency of the TLS routine. The number of candidates that passed this first selection is 48.

I performed a series of vetting tests on the light curves of these 48 candidate transiting objects: (i) inspection of the light curves obtained with different photometric apertures in order to check changes in the transit depths due to a close eclipsing binary; (ii) check of the light curves phased with a period of 0.5×, 1×, and 2× the period found by the TLS routine, in order to search for secondary eclipses; (iii) comparison between the binned even/odd folded transits, in order to check if the depth of the transits are in agreement within the errors; (iv) analysis of the in/out-of-transit difference centroid to check if the transit events are associated with a close contaminant. I refer the reader to Papers I and II for a detailed description of the vetting tests. Fig. 8 shows an overview of the main steps of the vetting procedure: the not-flattened light curve and the position of odd/even transits of the candidate TIC 143777072 are shown in panel (b); panels (c) illustrate the comparison between odd and even transits because the mean depths of the transits agree within the errors, the candidate passed this test; panel (d) shows the analysis of the in/out-of-transit difference centroid: in both the sectors in which the star was observed, the mean centroid is not located on the candidate but on a star (TIC 143777056) located at ∼50 arcsec from the target. I checked the light curve of the contaminant in the ASAS-SN archive. The result is reported in the inset of the panel (d): the contaminant is confirmed to be an eclipsing binary (depths of the primary eclipse $\delta_{\rm T} \sim 0.7$ mag in g band).

After the vetting procedure, nine objects of interest (PATHOS-35–43) belonging to two associations (Lup and Vel) survived. Among them, there are two *TESS* Objects of Interest (TOI)[10] released by the *TESS* team (TOI-580 = PATHOS-36, TOI-831 = PATHOS-41).

4.1 Stellar parameters

In order to extract physical parameters of the transiting objects from the light curves of their host, some star parameters, such as temperature, mass, and radius, are mandatory. I extracted the information for each star that hosts a candidate transiting exoplanet by fitting isochrones to the CMDs of the associations. Stellar parameters are derived interpolating the colour and the magnitude of the host star on the isochrone. For the isochrone fitting, I used the set of PARSEC isochrones, the distance modulus, the reddening, and the metallicity adopted in Section 3.1, and the ages derived in the same section. Stellar parameters for the host of transiting objects are reported in Table 2. These information are used for the transit modelling, as described in the next section.

4.2 Modelling of the transits

I used the PYTHON package `PYORBIT`[11] (Malavolta et al. 2016, 2018; Benatti et al. 2019), developed for the modelling of planetary transits and radial velocities. The routine is based on the combined use of the package `BATMAN` (Kreidberg 2015), the affine invariant Markov chain Monte Carlo sampler `EMCEE` (Foreman-Mackey et al. 2013), and the global optimization algorithm `PYDE`[12](Storn & Price 1997).

For the transit model, I included the central time of the first transit (T_0), the period (P), the impact parameter (b), the planetary-to-stellar-radius ratio ($R_{\rm P}/R_{\star}$), and the stellar density ($\rho_{\star}$). To locally model the stellar activity, for each transit a second-degree polynomial fit is performed to the out-of-transit part of the light curve. To take into account the impact of the dilution (df) on the error estimate of $R_{\rm P}$, I included in the modelling this quantity as a free parameter, with a Gaussian prior obtained using the stars in the *Gaia* DR2 catalogue that fall in the same pixel of the target, and transforming their *Gaia* magnitude in *TESS* magnitudes with the equations reported by Stassun et al. (2019). I extracted information on the limb-darkening (LD) coefficients using the $T_{\rm eff}$ and $\log(g)$ values obtained with the isochrone fitting, and the grid of values published by Claret (2018); the LD parametrization adopted is that described by Kipping (2013).

[9] `TLS v.1.0.24`; https://github.com/hippke/tls

[10] https://tess.mit.edu/toi-releases/go-to-alerts/

[11] https://github.com/LucaMalavolta/PyORBIT

[12] https://github.com/hpparvi/PyDE

Downloaded from https://academic.oup.com/mnras/article/498/4/5972/5903707 by guest on 13 May 2022

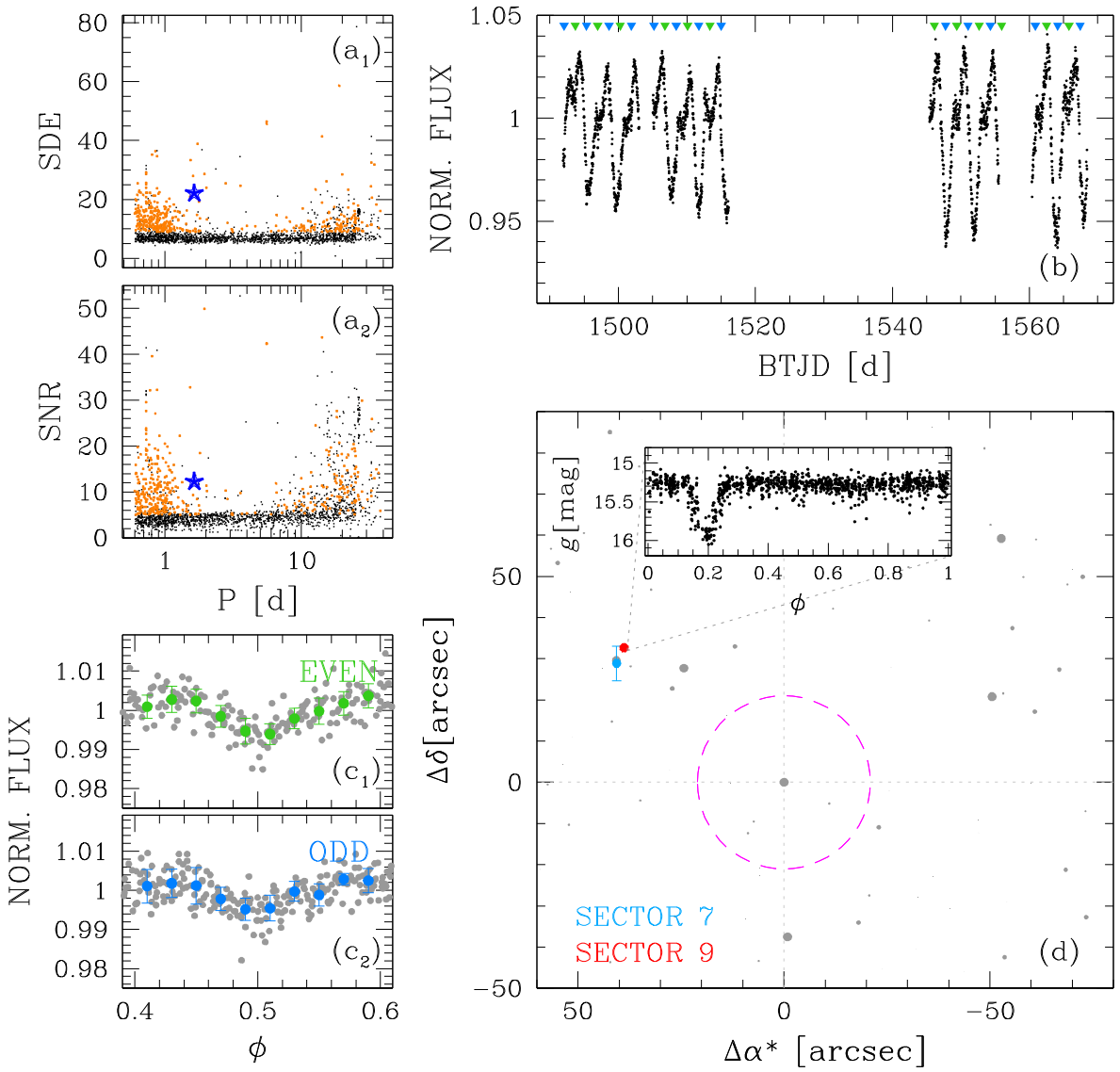


Figure 8. Overview on the selection of candidate transiting objects. Panels (a) show the SDE and SNR versus Period distributions obtained with the TLS routine; the blue star represents TIC 143777072. Panel (b) shows the light curve of TIC 143777072 observed in Sectors 7 and 9; the green and azure triangles indicate the even and odd transits, respectively. Panels (c) are the phased even and odd transits: the green/azure points are the median flux values calculated in bins of width 0.01. Panel (d) is the analysis of in/out-of-transit difference centroid: in (0,0) is located TIC 143777072; the magenta circle has the same size of the photometric aperture adopted in the light curve analysis; the light blue and red points are the mean centroids calculated for sectors 7 and 9, respectively, and indicate that the transit events happen on the suspected eclipsing binary TIC 143777056, whose ASAS-SN g-band light curve is plotted in the inset panel.

Table 2. Star parameters and priors for the modelling.

TIC	PATHOS	Assoc.	α (deg)	δ (deg)	T (mag.)	$R_\star$ ($R_\odot$)	$M_\star$ ($M_\odot$)	$\rho_\star$ ($\rho_\odot$)	Period (d)	T_0 (BTJD)	LD$_{c1}$	LD$_{c2}$	df
0081353413	35	Vel	123.0858	−47.0901	14.2	1.04 ± 0.15	0.72 ± 0.05	0.65 ± 0.17	$\mathcal{U}(1.9, 2.1)$	$\mathcal{U}(1492.0, 1493.0)$	0.38 ± 0.10	0.23 ± 0.10	0.43 ± 0.05
0081419525	36	Vel	123.1083	−46.1092	9.6	1.67 ± 0.01	2.35 ± 0.05	0.50 ± 0.01	$\mathcal{U}(1.4, 1.6)$	$\mathcal{U}(1517.0, 1519.0)$	0.15 ± 0.10	0.19 ± 0.10	0.16 ± 0.01
0095003423	37	Lup	242.5225	−31.4072	11.5	1.07 ± 0.10	0.77 ± 0.04	0.62 ± 0.10	$\mathcal{U}(1.4, 1.6)$	$\mathcal{U}(1630.0, 1631.0)$	0.44 ± 0.10	0.33 ± 0.10	0.05 ± 0.01
0123755508	38	Vel	115.8049	−47.7691	12.6	1.26 ± 0.10	1.13 ± 0.03	0.56 ± 0.08	$\mathcal{U}(15.0, 16.0)$	$\mathcal{U}(1492.0, 1493.0)$	0.41 ± 0.10	0.36 ± 0.10	0.11 ± 0.02
0238235254	39	Vel	119.8065	−49.9738	6.5	3.90 ± 0.10	8.25 ± 0.17	0.14 ± 0.01	$\mathcal{U}(5.4, 5.7)$	$\mathcal{U}(1497.0, 1498.0)$	0.02 ± 0.20	0.02 ± 0.20	0.50 ± 0.05
0238379370	40	Vel	120.7447	−49.0184	12.2	1.36 ± 0.11	1.23 ± 0.05	0.49 ± 0.07	$\mathcal{U}(27.0, 27.3)$	$\mathcal{U}(1511.5, 1512.0)$	0.38 ± 0.10	0.34 ± 0.10	0.04 ± 0.01
0307610438	41	Lup	229.0335	−38.8753	8.8	1.94 ± 0.12	1.55 ± 0.12	0.21 ± 0.03	$\mathcal{U}(1.4, 1.6)$	$\mathcal{U}(1601.5, 1602.5)$	0.33 ± 0.10	0.31 ± 0.10	0.01 ± 0.01
0374732772	42	Lup	242.1279	−38.4741	10.0	1.43 ± 0.09	1.26 ± 0.04	0.44 ± 0.05	$\mathcal{U}(17.5, 19.5)$	$\mathcal{U}(1631.0, 1632.0)$	0.39 ± 0.10	0.35 ± 0.10	0.05 ± 0.01
0411662605	43	Lup	244.4028	−50.3948	10.7	1.31 ± 0.08	1.13 ± 0.02	0.50 ± 0.05	$\mathcal{U}(1.4, 1.6)$	$\mathcal{U}(1631.0, 1632.0)$	0.42 ± 0.10	0.36 ± 0.10	0.07 ± 0.01

All the priors adopted for the modelling are listed in Table 2. For the modelling of the transits I adopted a circular orbit ($e = 0$). In the modelling process, the routine took into account of the 30-min cadence of the TESS time-series (Kipping 2010). The routine explored all the parameters in linear space, using a number of walkers $N_{\rm walkers}$ equal to 10 times the number of free parameters. For each model, I run the sampler for 80 000 steps, cutting away the first 15 000 steps as burn-in, and using a thinning factor of 100.

Downloaded from https://academic.oup.com/mnras/article/498/4/5972/5903707 by guest on 13 May 2022

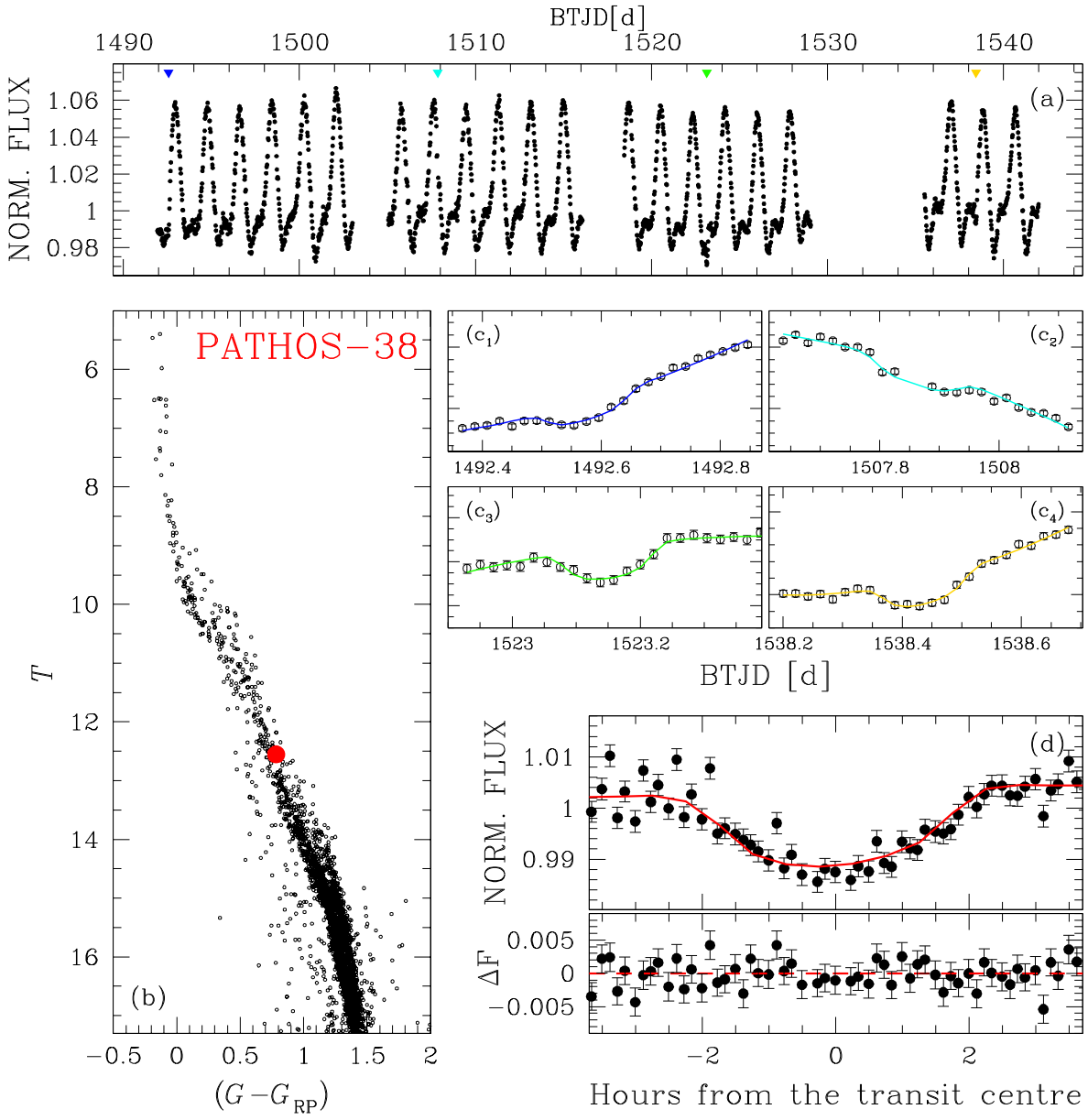


Figure 9. Overview on the modelling procedure adopted for deriving the physical parameters of the transiting object PATHOS-38. Panel (a) shows the light curve of PATHOS-38 (TIC 123755508), whose position in the T versus $G - G_{RP}$ CMD is shown with a red circle in panel (b). Panels (c) show the local polynomial fit + transit fit for each transit of the candidate exoplanet observed by *TESS*: the models are colour-coded as the arrows that indicate the epoch of the transit centres in panel (a). Panel (d) shows the folded transits (the black points) after removing the local polynomial fits: in red the mean model of the transits. Bottom panel shows the difference between the observed and the modelled transits (see text for details).

An overview on the modelling procedure is reported in Fig. 9 for PATHOS-38. The results of the modelling for all the objects of interest are reported in Table 3 and Figs 10 and 11.

4.3 Candidate exoplanets' frequency in young associations

In this work, I found and modelled nine transiting objects of interest. For the analysis described in this section, I excluded the objects with a radius $R_P \gtrsim 2\ R_J$ (PATHOS-37 and PATHOS-39), because of their doubtful planet nature. I excluded also PATHOS-43 because, on the basis of its position on the G versus $(G - G_{RP})$ CMD (see Fig. 11), it has a high probability to be not an association member.

All the six survived candidates I have detected are Jupiter size candidate exoplanets ($R_P \sim 0.9$–$1.6\ R_J$). No Neptune- or Earth-size candidate planets have been detected. Given the distance of the associations (∼150–400 pc) and the photometric precision of the light curves, on the basis of the analysis performed in Paper II (see Fig. 8), it is not possible to detect (super-)Earth size planets around association members studied in this work. On the basis of the same analysis, it is possible to detect Neptune-size exoplanets only for stars with radii $R_\star \lesssim 1.0\ R_\odot$. I calculated the expected number of exoplanets (N_{planet}) as done in Paper II, using the (modified) equation:

$$N_{planet} = f_\star \times \sum_r N_\star{}^r \times \mathrm{Pr}_{transit}{}^r, \quad (2)$$

where $f_\star$ is the percentage of stars with at least one exoplanet, the sum on r indicate the intervals of stellar radii considered [r = (0.0, 0.5), (0.5, 1.0), (1.0, 1.5), (1.5, 2.0) $R_\odot$], $N_\star$ is the number

Downloaded from https://academic.oup.com/mnras/article/498/4/5972/5903707 by guest on 13 May 2022

Table 3. Results of transit modelling.

TIC	PATHOS	Assoc.	P (d)	T_0 (BTJD)	$R_p/R_\star$	b	a (au)	$\rho_\star$ ($\rho_\odot$)	i (deg)	R_p (R_J)	R_p ($R_\oplus$)	Note
0081353413	35	Vel	$2.0865^{-0.0004}_{+0.0004}$	$1492.869^{-0.004}_{+0.003}$	$0.132^{-0.0069}_{+0.009}$	$0.31^{-0.21}_{+0.33}$	$0.0286^{-0.0007}_{+0.0006}$	$0.51^{-0.23}_{+0.13}$	$86.8^{-4.9}_{+2.2}$	$1.42^{-0.13}_{+0.42}$	$15.9^{-1.4}_{+4.7}$	
0081419525	36	Vel	$1.5498^{-0.0003}_{+0.0003}$	$1518.383^{-0.003}_{+0.003}$	$0.053^{-0.0017}_{+0.002}$	$0.37^{-0.16}_{+0.11}$	$0.0348^{-0.0002}_{+0.0002}$	$0.50^{-0.01}_{+0.01}$	$85.3^{-1.4}_{+2.1}$	$0.87^{-0.03}_{+0.03}$	$9.7^{-0.3}_{+0.3}$	(1)
0095003423	37	Lup	$1.5268^{-0.0003}_{+0.0003}$	$1630.461^{-0.003}_{+0.003}$	$0.202^{-0.0094}_{+0.011}$	$0.51^{-0.18}_{+0.13}$	$0.0238^{-0.0004}_{+0.0004}$	$0.58^{-0.12}_{+0.11}$	$83.7^{-2.2}_{+2.4}$	$2.16^{-0.20}_{+0.28}$	$24.2^{-2.2}_{+3.1}$	
0123755508	38	Vel	$15.2869^{-0.0020}_{+0.0020}$	$1492.575^{-0.004}_{+0.004}$	$0.128^{-0.0059}_{+0.007}$	$0.77^{-0.05}_{+0.05}$	$0.1256^{-0.0011}_{+0.0011}$	$0.52^{-0.09}_{+0.09}$	$87.9^{-0.3}_{+0.2}$	$1.61^{-0.13}_{+0.19}$	$18.1^{-1.5}_{+2.1}$	
0238235254	39	Vel	$5.5705^{-0.0004}_{+0.0004}$	$1497.200^{-0.003}_{+0.003}$	$0.127^{-0.0166}_{+0.015}$	$0.97^{-0.02}_{+0.02}$	$0.1243^{-0.0009}_{+0.0008}$	$0.14^{-0.01}_{+0.01}$	$81.9^{-0.3}_{+0.3}$	$4.78^{-0.65}_{+0.59}$	$53.6^{-7.3}_{+6.6}$	(2)
0238379370	40	Vel	$27.1769^{-0.0072}_{+0.0067}$	$1511.748^{-0.009}_{+0.009}$	$0.079^{-0.0089}_{+0.018}$	$0.89^{-0.05}_{+0.05}$	$0.1895^{-0.0026}_{+0.0025}$	$0.49^{-0.07}_{+0.07}$	$88.3^{-0.2}_{+0.1}$	$1.05^{-0.14}_{+0.27}$	$11.8^{-1.5}_{+3.0}$	
0307610438	41	Lup	$1.5615^{-0.0003}_{+0.0003}$	$1601.955^{-0.002}_{+0.002}$	$0.072^{-0.0026}_{+0.003}$	$0.80^{-0.04}_{+0.04}$	$0.0305^{-0.0008}_{+0.0008}$	$0.20^{-0.03}_{+0.03}$	$76.1^{-1.5}_{+1.3}$	$1.38^{-0.10}_{+0.13}$	$15.5^{-1.2}_{+1.4}$	(1)
0374732772	42	Lup	$18.7944^{-0.0092}_{+0.0042}$	$1632.117^{-0.012}_{+0.015}$	$0.077^{-0.0120}_{+0.018}$	$0.77^{-0.21}_{+0.13}$	$0.1494^{-0.0016}_{+0.0016}$	$0.44^{-0.05}_{+0.05}$	$88.0^{-0.4}_{+0.5}$	$1.06^{-0.17}_{+0.26}$	$11.9^{-1.9}_{+3.0}$	(3)
0411662605	43	Lup	$1.5610^{-0.0006}_{+0.0006}$	$1631.386^{-0.004}_{+0.005}$	$0.056^{-0.0023}_{+0.002}$	$0.17^{-0.12}_{+0.16}$	$0.0274^{-0.0002}_{+0.0002}$	$0.47^{-0.05}_{+0.05}$	$87.8^{-2.1}_{+1.5}$	$0.73^{-0.04}_{+0.04}$	$8.2^{-0.4}_{+0.4}$	(4)

Notes.(1) Also in the TOI catalogue.
(2) Radius too large, suspected eclipsing binary.
(3) Another single deeper (suspected) transit ($\delta_T \sim 5$ %) is present in the light curve due to a likely stellar companion or second planet.
(4) Likely field star.

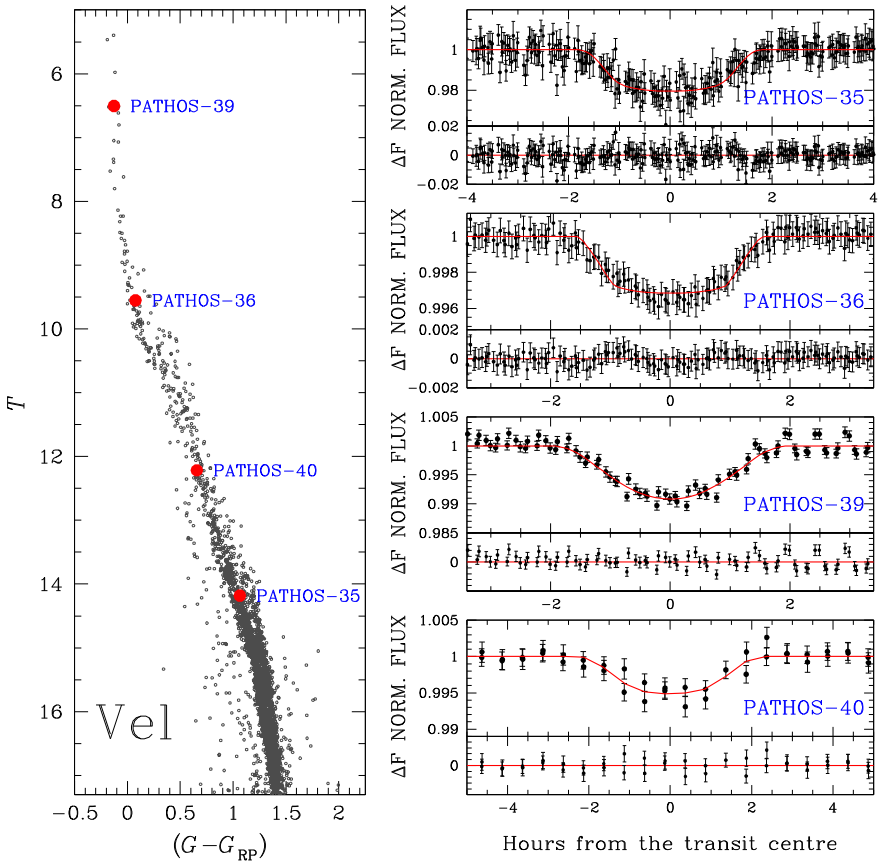


Figure 10. Overview on the transiting objects (PATHOS-35, 36, 39, and 40) orbiting Vel association stars. Left panel shows the G versus $(G - G_{RP})$ CMD of the likely Vel members: the red dots indicate the transiting objects' positions. Right-hand panels show the phased transits of the objects of interest and the fitted transit models (red); for each object, the difference between the observations and the model is shown below its folded light curve.

of stars in the considered stellar radius bins, $Pr_{transit} \simeq R_\star/a$ is the transit probability, with a the semimajor axis of the orbit, calculated using the third law of Kepler and using an average period $P = 10$ d. Considering (1) the stars for which I analysed the light curves, (2) the stars with $R_\star \leq 1 R_\odot$, (3) the frequencies $f_\star$ for Neptune-size exoplanets tabulated by Fressin et al. (2013) in the case of exoplanets with $P = 0.8 - 10.0$ d (∼0.21 per cent) and calculated in Paper II (∼1.34 per cent), I expect to find $N_{planet}(R_P = 1\ R_N) = 1 \pm 1$, in agreement with the null detection found in this work.

The Jupiter-size candidates found in this work orbit stars in the Lup (2 candidates) and Vel (4 candidates) associations, the oldest associations studied in this work, while no candidates have been found around ChI, ChII, and CrA associations. Using equation (2), I calculated the frequency of candidate Jupiters in Lup and Vel associations. Because the periods of the candidates range between ∼1.5 and ∼27 d, I divided the sample of candidate exoplanets in three sub-samples and, on the basis of their periods, I calculated the frequency $f_\star$ using the transit probabilities associated with the mean period $\bar{P}$ of the candidates that form the sub-sample:

Downloaded from https://academic.oup.com/mnras/article/498/4/5972/5903707 by guest on 13 May 2022

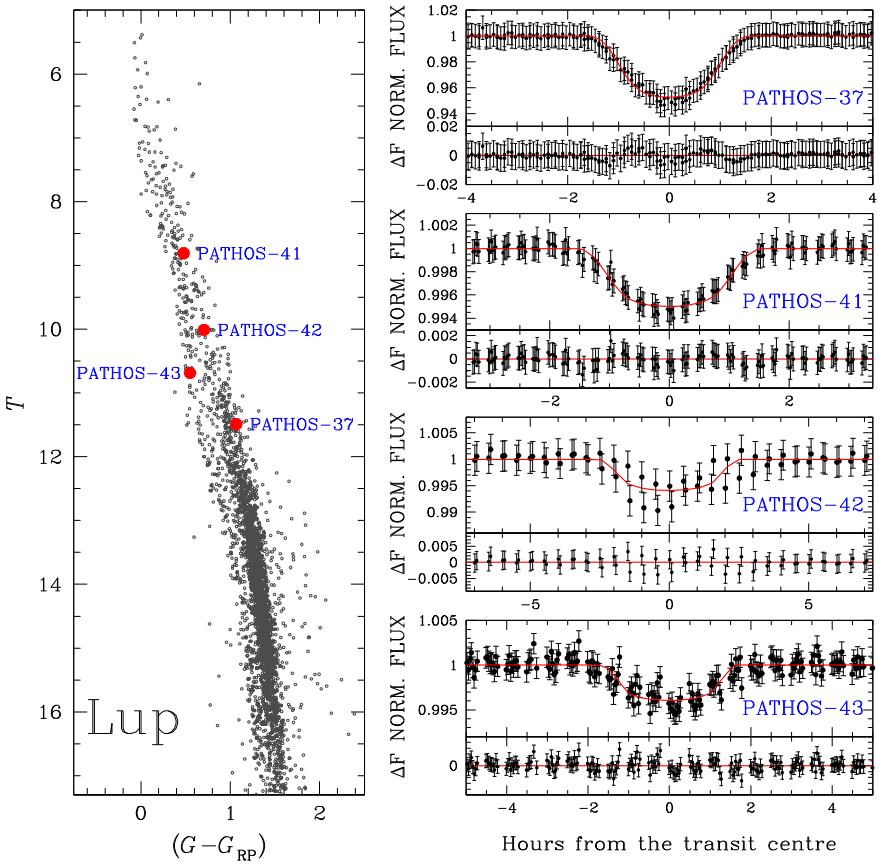


Figure 11. As in Fig. 10, but for objects of interest that are likely members of Lup association (PATHOS-37, 41, 42, 43).

(i) for candidates with period 1.0 d $\leq P \leq$ 2.1 d, ($\bar{P} \sim$ 1.7 d) I found $f_\star = (0.70 \pm 0.70)$ per cent and $f_\star = (0.44 \pm 0.31)$ per cent, for Lup and Vel association, respectively; considering all the stars analysed in this work (i.e. including also the ChI, ChII, and CrA members), I found $f_\star = (0.43 \pm 0.25)$ per cent. For giant planets orbiting field stars with periods 0.8 d $\leq P \leq$ 2.0 d, Fressin et al. (2013) tabulated a frequency of $f_\star = (0.015 \pm 0.007)$ per cent, that is lower than the mean values found in this work but in agreement within $\sim 2\sigma$;

(ii) for candidates with period 15.0 d $\leq P \leq$ 30 d ($\bar{P} \sim$ 20.3 d) I found $f_\star = (3.64 \pm 3.64)$ per cent, $f_\star = (2.28 \pm 1.63)$ per cent, and $f_\star = (2.24 \pm 1.31)$ per cent if I consider only Lup members, Vel members, and all the stars, respectively. For Jupiter exoplanets orbiting field stars with period in the range 17.0 d $\leq P \leq$ 29.0 d, Fressin et al. (2013) found a frequency $f_\star = (0.23 \pm 0.12)$ per cent; also in this case the mean frequency found in this work is higher than that tabulated by Fressin et al. (2013), even if they agree within 2σ.

(iii) for candidates with period 1.0 d $\leq P \leq$ 30 d ($\bar{P} \sim$ 11.0 d) the frequencies of Jupiter-size exoplanets in the Lup and Vel members are $f_\star = (4.84 \pm 3.51)$ per cent and $f_\star = (3.03 \pm 1.54)$ per cent, respectively. Considering all the stars analysed in this work, I found a frequency $f_\star = (2.99 \pm 1.24)$ per cent. Fressin et al. (2013) found for giant planets around field stars with periods 0.8 d $\leq P \leq$ 29.0 d a frequency $f_\star = (0.93 \pm 0.10)$ per cent, also in this case lower than the value found in this work, but in agreement within 2σ.

I want to emphasize that, for the statistical analysis performed in this work, the completeness of the detection method was not taken into account, and therefore the calculated frequencies might be considered as lower limits.

Using the results previously obtained, I calculated how many transiting Jupiters are expected to be found in the others three associations: even considering the maximum mean frequency found in the previous analysis (~4.8 per cent), the expected number of giants in the three associations is $N_P < 1$, in agreement with the null detection obtained in this work.

5 SUMMARY AND CONCLUSIONS

In this work, the third of the PATHOS project, I performed a detailed analysis of the light curves of stars in five young (*T*-)associations associated with star-forming regions: Chamaeleon I and II, Lupus, Corona Australis, and γ Velorum association. These associations have been chosen because of their young age ($\lesssim$10 Myr): indeed, searching and characterizing exoplanets orbiting very young stars allow us to constraint theoretical models on the formation of them and to understand the mechanisms that prevail in their dynamical and physical evolution (migration, atmospheric loss, etc.).

For this work, I extracted and corrected 7150 light curves of 4459 association members from *TESS* FFIs using the PSF-based approach pipeline already adopted with success in previous works. Light curves will be publicly available as HLSP on the PATHOS project webpage[13](DOI: 10.17909/t9-es7m-vw14) of the MAST archive.

By performing an analysis of the GLS periodograms of the light curves, I identified 1260 periodic variable stars. Combining the gyrochronological analysis of periodic variable stars and the isochrone

[13]https://archive.stsci.edu/hlsp/pathos

Downloaded from https://academic.oup.com/mnras/article/498/4/5972/5903707 by guest on 13 May 2022

fitting of the CMD, I constrained the ages of the associations, obtaining that the five associations have ages that span between ∼2 and ∼10 Myr. Because of the young age, the analysed associations host a large number of YSOs surrounded by circumstellar disc. By the analysis of the light curves, I identified 71 dipper stars, i.e. stars that present in their light curves important drops of the flux on time-scales of $\lesssim$1 d. These drops of the luminosity are due to the dust that form the inner regions of the circumstellar discs; comparing the simultaneous drops observed in *TESS* and *g*-band ASAS-SN light curves, I calculated the ratio between the absorptions in *T* and *g* bands (A_T/A_g), which gives us information on the size of the grains that form the disc. In particular, when $A_T/A_g \rightarrow 1$ the grains have sizes comparable with the wavelengths in which *TESS* observes; lower values of the ratio A_T/A_g are associated with smaller grains. I found a weak anticorrelation between A_T/A_g and the dereddened colour $(V - K)_0$, with grain sizes that decrease with the mass of the hosting star. This work can not confirm the correlation between the infrared excess (K_s − [22 μm]) and A_T/A_g found by Bredall et al. (2020). Finally, I found that the highest frequency of dippers are associated with the low-mass stars of the youngest associations (ChI and ChII, ∼2.5 Myr, frequency ∼20 per cent), and that the frequency of dippers is anticorrelated with the age of the associations, confirming that the time-scales for the disc cleaning around low-mass stars is <10 Myr (Luhman & Mamajek 2012).

I searched for transit signals among the light curves of the association members, and after the vetting tests (analysis of the odd/even transits, of the in-/out-of transit centroid offset, etc.), nine objects of interest passed the selections. In order to derive the physical parameters of the transiting objects, I modelled their transits using their light curves and the stellar parameters derived through isochrone fits. Excluding two objects of interest, because their radius is too large ($R_P > 2R_J$), and another object of interest because hosted by a likely field star, I detected six Jupiter size candidates: two in the Lup association and four in the Vel association. No Earth-, super-Earth-, and Neptune-size candidates have been detected; anyway, given the distance of the associations, the number of members, and the frequency of these kind of exoplanets tabulated by Fressin et al. (2013) and in Paper II, the null detection is agreement with the expectations. The mean frequency of giant planets in associations derived considering different period intervals ranges between ∼1 per cent and ∼4 per cent, higher than the values reported by Fressin et al. (2013) for giants orbiting field stars ($\lesssim$1 per cent) and in Paper II for Jupiters orbiting open cluster members (∼0.20 per cent). Anyway, given the low number of candidates, the errors on the calculated frequencies are too large, and the obtained results must be considered provisional. I also verified if the null detection of giant planets around ChI, ChII, and CrA members is expected: even considering a frequency $f_\star$ ∼5 per cent, the number of Jupiter size exoplanet expected is $N_P < <1$, in agreement with the null detection of this work.

The analysis of the light curves of older association members (∼10–100 Myr), targets of next works of the PATHOS project, is mandatory to understand if the frequency and/or the orbital and physical parameters of the exoplanets are correlated with the age of the hosting stars. In this way, it will be possible understand how exoplanets born, and trace the prevailing mechanisms that characterize their life.

ACKNOWLEDGEMENTS

I acknowledge the support from the French Centre National d'Etudes Spatiales (CNES). I acknowledge the partial support from PLATO ASI-INAF agreements n. 2015-019-R0-2015 and 2015-019-R.1-2018. I warmly thank the referee for carefully reading the manuscript. I thank M. Deleuil and G. Piotto for the useful suggestions on this work, and L. Malavolta for his support in the use of PYORBIT. This paper includes data collected by the *TESS* mission. Funding for the *TESS* mission is provided by the NASA Explorer Program. This work has used data from the European Space Agency (ESA) mission *Gaia* (https://www.cosmos.esa.int/gaia), processed by the *Gaia* Data Processing and Analysis Consortium (DPAC, https://www.cosmos.esa.int/web/gaia/dpac/consortium). Funding for the DPAC has been provided by national institutions, in particular the institutions participating in the *Gaia* Multilateral Agreement. Some tasks of the data analysis have been carried out using VARTOOLS v 1.38 (Hartman & Bakos 2016) and TLS PYTHON routine (Hippke & Heller 2019).

DATA AVAILABILITY

The data underlying this article are available in MAST at doi:10.17909/t9-es7m-vw14 and at https://archive.stsci.edu/hlsp/pathos.

The data underlying this article are available in the article and in its online supplementary material.

REFERENCES

Aizawa M., Suto Y., Oya Y., Ikeda S., Nakazato T., 2020, ApJ, 899, 55
Ambartsumian V. A., 1949, Astron. Zh., 26, 3
Ansdell M. et al., 2016, ApJ, 816, 69
Baraffe I., Chabrier G., Barman T. S., Allard F., Hauschildt P. H., 2003, A&A, 402, 701
Barnes S. A., 2003, ApJ, 586, 464
Barnes S. A., 2007, ApJ, 669, 1167
Barros S. C. C., Demangeon O., Deleuil M., 2016, A&A, 594, A100
Benatti S. et al., 2019, A&A, 630, A81
Biazzo K., Randich S., Palla F., Briceño C., 2011, A&A, 530, A19
Biazzo K., D'Orazi V., Desidera S., Covino E., Alcalá J. M., Zusi M., 2012a, MNRAS, 427, 2905
Biazzo K., Alcalá J. M., Covino E., Frasca A., Getman F., Spezzi L., 2012b, A&A, 547, A104
Bodman E. H. L. et al., 2017, MNRAS, 470, 202
Bohn A. J. et al., 2019, A&A, 624, A87
Borucki W. J. et al., 2010, Science, 327, 977
Bouma L. G., Hartman J. D., Bhatti W., Winn J. N., Bakos G. Á., 2019, ApJS, 245, 13
Bovy J., Rix H.-W., Green G. M., Schlafly E. F., Finkbeiner D. P., 2016, ApJ, 818, 130
Bredall J. W. et al., 2020, MNRAS, 496, 3257
Bressan A., Marigo P., Girardi L., Salasnich B., Dal Cero C., Rubele S., Nanni A., 2012, MNRAS, 427, 127
Carpenter J. M., Mamajek E. E., Hillenbrand L. A., Meyer M. R., 2006, ApJ, 651, L49
Carpenter J. M., Mamajek E. E., Hillenbrand L. A., Meyer M. R., 2009, ApJ, 705, 1646
Chen C. H., Jura M., Gordon K. D., Blaylock M., 2005, ApJ, 623, 493
Chen C. H., Mamajek E. E., Bitner M. A., Pecaut M., Su K. Y. L., Weinberger A. J., 2011, ApJ, 738, 122
Ciardi D. R. et al., 2018, AJ, 155, 10
Claret A., 2018, A&A, 618, A20
Cody A. M. et al., 2014, AJ, 147, 82
Cody A. M., Hillenbrand L. A., 2010, ApJS, 191, 389
Cody A. M., Hillenbrand L. A., 2018, AJ, 156, 71
Curtis J. L. et al., 2018, AJ, 155, 173
Curtis J. L., Agüeros M. A., Mamajek E. E., Wright J. T., Cummings J. D., 2019, AJ, 158, 77
Cutri R. M., et al., 2003, The IRSA 2MASS All-Sky Point Source Catalog, NASA/IPAC Infrared Science Archive.

Downloaded from https://academic.oup.com/mnras/article/498/4/5972/5903707 by guest on 13 May 2022

D'Orazi V., Randich S., Flaccomio E., Palla F., Sacco G. G., Pallavicini R., 2009, A&A, 501, 973
D'Orazi V., Biazzo K., Randich S., 2011, A&A, 526, A103
David T. J. et al., 2016a, AJ, 151, 112
David T. J. et al., 2016b, Nature, 534, 658
David T. J. et al., 2018, AJ, 156, 302
David T. J. et al., 2019a, AJ, 158, 79
David T. J., Petigura E. A., Luger R., Foreman-Mackey D., Livingston J. H., Mamajek E. E., Hillenbrand L. A., 2019b, ApJ, 885, L12
Drimmel R., Cabrera-Lavers A., López-Corredoira M., 2003, A&A, 409, 205
Foreman-Mackey D., Hogg D. W., Lang D., Goodman J., 2013, PASP, 125, 306
Fressin F. et al., 2013, ApJ, 766, 81
Fulton B. J. et al., 2017, AJ, 154, 109
Fulton B. J., Petigura E. A., 2018, AJ, 156, 264
Gaia Collaboration, 2018, A&A, 616, A1
Gaidos E. et al., 2020, MNRAS, 495, 650
Girardi L., Bertelli G., Bressan A., Chiosi C., Groenewegen M. A. T., Marigo P., Salasnich B., Weiss A., 2002, A&A, 391, 195
González Hernández J. I., Caballero J. A., Rebolo R., Béjar V. J. S., Barrado Y Navascués D., Martín E. L., Zapatero Osorio M. R., 2008, A&A, 490, 1135
Green G. M., Schlafly E., Zucker C., Speagle J. S., Finkbeiner D., 2019, ApJ, 887, 93
Hansen B. M. S., Murray N., 2012, ApJ, 751, 158
Hartman J. D., Bakos G. Á., 2016, Astron. Comput., 17, 1
Hippke M., Heller R., 2019, A&A, 623, A39
Howell S. B. et al., 2014, PASP, 126, 398
Ida S., Lin D. N. C., 2010, ApJ, 719, 810
James D. J., Melo C., Santos N. C., Bouvier J., 2006, A&A, 446, 971
Jeffries R. D. et al., 2017, MNRAS, 464, 1456
Kipping D. M., 2010, MNRAS, 408, 1758
Kipping D. M., 2013, MNRAS, 435, 2152
Kochanek C. S. et al., 2017, PASP, 129, 104502
Kreidberg L., 2015, PASP, 127, 1161
Kuruwita R. L., Ireland M., Rizzuto A., Bento J., Federrath C., 2018, MNRAS, 480, 5099
Libralato M. et al., 2016b, MNRAS, 463, 1780
Libralato M., Bedin L. R., Nardiello D., Piotto G., 2016a, MNRAS, 456, 1137
Lindegren L. et al., 2018, A&A, 616, A2
Lopez E. D., Fortney J. J., 2013, ApJ, 776, 2
Luhman K. L., Mamajek E. E., 2012, ApJ, 758, 31
Malavolta L. et al., 2016, A&A, 588, A118
Malavolta L. et al., 2018, AJ, 155, 107
Mann A. W. et al., 2016a, AJ, 152, 61
Mann A. W. et al., 2016b, ApJ, 818, 46
Mann A. W. et al., 2018, AJ, 155, 4
Marigo P. et al., 2017, ApJ, 835, 77
Marley M. S., Fortney J. J., Hubickyj O., Bodenheimer P., Lissauer J. J., 2007, ApJ, 655, 541
Marshall D. J., Robin A. C., Reylé C., Schultheis M., Picaud S., 2006, A&A, 453, 635
Meibom S. et al., 2013, Nature, 499, 55
Morales-Calderón M. et al., 2011, ApJ, 733, 50
Mordasini C., Marleau G. D., Mollière P., 2017, A&A, 608, A72
Nardiello D. et al., 2015a, MNRAS, 447, 3536
Nardiello D. et al., 2015b, MNRAS, 451, 312
Nardiello D. et al., 2019, MNRAS, 490, 3806 (Paper I)
Nardiello D. et al., 2020, MNRAS, 495, 4924 (Paper II)
Nardiello D., Libralato M., Bedin L. R., Piotto G., Ochner P., Cunial A., Borsato L., Granata V., 2016a, MNRAS, 455, 2337
Nardiello D., Libralato M., Bedin L. R., Piotto G., Borsato L., Granata V., Malavolta L., Nascimbeni V., 2016b, MNRAS, 463, 1831
Newton E. R. et al., 2019, ApJ, 880, L17
Obermeier C. et al., 2016, AJ, 152, 223
Owen J. E., Lai D., 2018, MNRAS, 479, 5012
Owen J. E., Wu Y., 2013, ApJ, 775, 105
Pecaut M. J., Mamajek E. E., 2013, ApJS, 208, 9
Pecaut M. J., Mamajek E. E., Bubar E. J., 2012, ApJ, 746, 154
Pepper J. et al., 2017, AJ, 153, 177
Pope B. J. S., Parviainen H., Aigrain S., 2016, MNRAS, 461, 3399
Quinn S. N. et al., 2012, ApJ, 756, L33
Quinn S. N. et al., 2014, ApJ, 787, 27
Rebull L. M. et al., 2016, AJ, 152, 114
Rebull L. M., Stauffer J. R., Cody A. M., Hillenbrand L. A., David T. J., Pinsonneault M., 2018, AJ, 155, 196
Rebull L. M., Stauffer J. R., Cody A. M., Hillenbrand L. A., Bouvier J., Roggero N., David T. J., 2020, AJ, 159, 273
Ricker G. R. et al., 2015, J. Astron. Telesc. Instrum. Syst., 1, 014003
Rizzuto A. C. et al., 2020, AJ, 160, 33
Rodriguez J. E. et al., 2017, ApJ, 848, 97
Santos N. C., Melo C., James D. J., Gameiro J. F., Bouvier J., Gomes J. I., 2008, A&A, 480, 889
Schlichting H. E., 2018, Handbook of Exoplanets, Formation of Super-Earths, Springer, Cham, p. 141
Schlichting H. E., Sari R., Yalinewich A., 2015, Icarus, 247, 81
Shappee B. J. et al., 2014, ApJ, 788, 48
Sokolovsky K. V. et al., 2017, MNRAS, 464, 274
Spiegel D. S., Burrows A., 2012, ApJ, 745, 174
Spina L. et al., 2014a, A&A, 567, A55
Spina L. et al., 2014b, A&A, 568, A2
Stassun K. G. et al., 2019, AJ, 158, 138
Stauffer J. et al., 2015, AJ, 149, 130
Storn R., Price K., 1997, J. Glob. Optim., 11, 341
Terquem C., Papaloizou J. C. B., 2007, ApJ, 654, 1110
Vanderburg A. et al., 2018, AJ, 156, 46
Wright E. L. et al., 2010, AJ, 140, 1868
Zechmeister M., Kürster M., 2009, A&A, 496, 577

SUPPORTING INFORMATION

Supplementary data are available at *MNRAS* online.

pathos3em.tar.gz

Please note: Oxford University Press is not responsible for the content or functionality of any supporting materials supplied by the authors. Any queries (other than missing material) should be directed to the corresponding author for the article.

APPENDIX A: ELECTRONIC MATERIAL

The catalogues of the periodic variable stars and of the dippers analysed in this work are available electronically as supporting material to this paper. Both the catalogues are in `ascii` and `fits` format. A description of the columns for the two catalogues are reported in Tables A1 and A2.

Light curves extracted and analysed in this work are available in the MAST archive as HLSP under the project PATHOS[14] (DOI: 10.17909/t9-es7m-vw14). The updated list of candidate exoplanets is reported on the PATHOS webpage of the MAST archive.

[14] https://archive.stsci.edu/hlsp/pathos

Downloaded from https://academic.oup.com/mnras/article/498/4/5972/5903707 by guest on 13 May 2022

Table A1. Description of the column content of the catalogue of variable stars.

Column	Name	Unit	Explanation
01	RA	(deg)	Right ascension (J2000, epoch 2015.5)
02	DEC	(deg)	Declination (J2000, epoch 2015.5)
03	TIC		*TESS* Input Catalogue ID
04	GAIA_DR2		*Gaia* DR2 Source ID
05	PERIOD	(d)	Period
06	Gmag	(mag)	*Gaia* DR2 G magnitude
07	e_Gmag	(mag)	Error on *Gaia* DR2 G magnitude
08	BPmag	(mag)	*Gaia* DR2 G_{BP} magnitude
09	e_BPmag	(mag)	Error on *Gaia* DR2 G_{BP} magnitude
10	RPmag	(mag)	*Gaia* DR2 G_{RP} magnitude
11	e_RPmag	(mag)	Error on *Gaia* DR2 G_{RP} magnitude
12	Tmag	(mag)	*TESS* T magnitude
13	e_Tmag	(mag)	Error on *TESS* T magnitude
14	Bmag	(mag)	B-Johnson magnitude
15	e_Bmag	(mag)	Error on B-Johnson magnitude
16	Vmag	(mag)	V-Johnson magnitude
17	e_Vmag	(mag)	Error on V-Johnson magnitude
18	Jmag	(mag)	2MASS J magnitude
19	e_Jmag	(mag)	Error on 2MASS J magnitude
20	Hmag	(mag)	2MASS H magnitude
21	e_Hmag	(mag)	Error on 2MASS H magnitude
22	Kmag	(mag)	2MASS K_s magnitude
23	e_Kmag	(mag)	Error on 2MASS K_s magnitude
24	W1mag	(mag)	WISE W_1 magnitude
25	e_W1mag	(mag)	Error on WISE W_1 magnitude
26	W2mag	(mag)	WISE W_2 magnitude
27	e_W2mag	(mag)	Error on WISE W_2 magnitude
28	W3mag	(mag)	WISE W_3 magnitude
29	e_W3mag	(mag)	Error on WISE W_3 magnitude
30	W4mag	(mag)	WISE W_4 magnitude
31	e_W4mag	(mag)	Error on WISE W_4 magnitude
32	E_BV		$E(B-V)$
33	PARALLAX	(mas)	Parallax from *Gaia* DR2
34	PM_RA	(mas yr^{-1})	Proper motion along the RA direction from *Gaia* DR2
35	PM_DEC	(mas yr^{-1})	Proper motion along the Dec. direction from *Gaia* DR2
36	ASSOCIATION		Name of the association that host the star

Table A2. Description of the column content of the catalogue of dipper stars.

Column	Name	Unit	Explanation
01	RA	(deg)	Right ascension (J2000, epoch 2015.5)
02	DEC	(deg)	Declination (J2000, epoch 2015.5)
03	TIC		*TESS* Input Catalogue ID
04	GAIA_DR2		*Gaia* DR2 Source ID
05	AT_AG		A_T/A_g values [−99.9: not available]
06	e_ATAG		Error on A_T/A_g values [−99.9: not available]
07	Gmag	(mag)	*Gaia* DR2 G magnitude
08	e_Gmag	(mag)	Error on *Gaia* DR2 G magnitude
09	BPmag	(mag)	*Gaia* DR2 G_{BP} magnitude
10	e_BPmag	(mag)	Error on *Gaia* DR2 G_{BP} magnitude
11	RPmag	(mag)	*Gaia* DR2 G_{RP} magnitude
12	e_RPmag	(mag)	Error on *Gaia* DR2 G_{RP} magnitude
13	Tmag	(mag)	*TESS* T magnitude
14	e_Tmag	(mag)	Error on *TESS* T magnitude
15	Bmag	(mag)	B-Johnson magnitude
16	e_Bmag	(mag)	Error on B-Johnson magnitude
17	Vmag	(mag)	V-Johnson magnitude
18	e_Vmag	(mag)	Error on V-Johnson magnitude
19	Jmag	(mag)	2MASS J magnitude
20	e_Jmag	(mag)	Error on 2MASS J magnitude
21	Hmag	(mag)	2MASS H magnitude
22	e_Hmag	(mag)	Error on 2MASS H magnitude
23	Kmag	(mag)	2MASS K_s magnitude

Downloaded from https://academic.oup.com/mnras/article/498/4/5972/5903707 by guest on 13 May 2022

Table A2 – *continued*

Column	Name	Unit	Explanation
24	e_Kmag	(mag)	Error on 2MASS K_s magnitude
25	W1mag	(mag)	WISE W_1 magnitude
26	e_W1mag	(mag)	Error on WISE W_1 magnitude
27	W2mag	(mag)	WISE W_2 magnitude
28	e_W2mag	(mag)	Error on WISE W_2 magnitude
29	W3mag	(mag)	WISE W_3 magnitude
30	e_W3mag	(mag)	Error on WISE W_3 magnitude
31	W4mag	(mag)	WISE W_4 magnitude
32	e_W4mag	(mag)	Error on WISE W_4 magnitude
33	E_BV		$E(B-V)$
34	PARALLAX	(mas)	Parallax from *Gaia* DR2
35	PM_RA	(mas yr^{-1})	Proper motion along the RA direction from *Gaia* DR2
36	PM_DEC	(mas yr^{-1})	Proper motion along the Dec. direction from *Gaia* DR2
37	ASSOCIATION		Name of the association that host the star

This paper has been typeset from a TEX/LATEX file prepared by the author.

Downloaded from https://academic.oup.com/mnras/article/498/4/5972/5903707 by guest on 13 May 2022